Memoirs of the Faculty of Science, Kyoto University, Series of Physics, Astrophysics, Geophysics and Chemistry, Vol. XXXVI, No. 1, Article 4, 1981

MEASUREMENT OF THE DIFFERENTIAL CROSS SECTIONS FOR THE $\pi^-p\to\pi^0n$ CHARGE EXCHANGE SCATTERING IN THE MOMENTUM REGION BETWEEN 1969 MeV/c AND 2965 MeV/c

By

Yoichiro SUZUKI

Department of Physics, Faculty of Science, Kyoto University, Kyoto

(*Received March 10, 1979*)

ABSTRACT

The differential cross sections for the $\pi^-p\to\pi^0n$ change exchange scattering at six incident pion momenta from 1969 MeV/c to 2965 MeV/c have been measured in the angular range between $\cos\theta^*=-0.95$ and $\cos\theta^*=+0.95$. The results are compared with those of other experiments and the predictions of the partial wave analyses.

I. Introduction

Pion-nucleon interactions are the most fundamental interactions to study the strong interactions and have been studied vigourously so far. Many πN resonances have been found by experimental studies and phase shift analyses during last two decades. Those informations have made tremendous contribution to develop the theories for understanding the structure of elementary particles, such as the quark models. The baryon resonances are fairly well understood in terms of three quarks, and the present status of the development of the quark models is summarized in many reports[1].

According to the recent πN phase shift analyses of Saclay 74[2], CMU–LBL 78[3], Karlsruhe-Helsinki 78[4] and Hendry[5], in the low mass region below 1800 MeV, the phase shifts are fairly well known, and the properties of a number of πN resonances are well established. These πN resonances are assigned to the multiplets predicted by the SU(6)×O(3) model. The mass ordering of the SU(6)×O(3) multiplets are listed in Table I–1).

Table I–1. Mass ordering of SU(6)×0(3) multiplets calculated by assuming the harmonic oscillator forces. (Ref. 1)

N	multiplet
0	$[56,0^+]$
1	$[70,1^-]$
2	$[56,2^+]$, $[70,0^+]$, $[70,2^+]$, $[56,0^+]'$
3	$[70,3^-]$, $[56,1^-]$, $[70,1^-]'$
4	$[56,4^+]$, $[56,2^+]'$, $[70.0^+]'$, $[70.2^+]'$, $[56,0^+]''$
⋮	

The N indicates the excitation number of the quanta.

The low mass multiplets of [56, 0^+], [70, 1^-] and [56, 2^+] are firmly established and almost all states have been observed. In the higher mass region, high spin multiplets of [70, 3^-] and [56, 4^+], and radial excitation multiplets of [56, 0^+]′ have been established, but only few states have been observed. The G_{17} (2190), G_{19} (2200) and G_{37} (2215) resonances are considered to be the candidates of [70, 3^-] multiplets. The H_{19} (2200) and H_{311} (2420) resonances are considered to be the candidates of [56, 4^+] multiplets. However, there are another possibility of finding high mass low spin multiplets of [56, 1^-], [70, 0^+] and [70, 2^+]. The S_{31} (2150) and D_{35} (1930)

Table I–2. SU(6)×O(3) Classification of Nucleon Resonances.

[56,0+]	P_{11}^{****}	P_{11}^{****}	P_{11}	D_{33}^{****}	D_{33}			
Saclay 76	938	1435	(1929)	1231				
CMU-LBL76	938	1467	1810	1233	1690			
CMU-LBL78	938	1450		1234	1640			
K-H 78	938	1410	(1723)	1233				
[56,2+]	P_{13}^{***}	F_{15}^{****}	F_{15}	P_{31}^{****}	P_{33}^{***}	F_{35}^{****}	F_{37}^{****}	
Saclay 76	1696	1679		1789	1900	1869	1928	
CMU-LBL76	1860	1684	1965	1940	2130	1885	1945	
CMU-LBL78	1740	1680		1920	1960	1920	1950	
K-H 78	1710	1684		1888	1868	1905	1913	
[56,4+]	F_{17}^{**}	H_{19}^{***}		F_{35}	F_{37}	H_{39}	H_{311}^{***}	
Saclay 76	2049	2249					2392	
CMU-LBL76	1965	2260						
CMU-LBL78	(2100)	(2250)						
K-H 78	2005	2205			2425	2217	2416	
[56,6+]	H_{111}	K_{113}		H_{39}	H_{311}	K_{313}	K_{315}	
K-H 78		2612					2990	
[56,1-]	S_{11}^{*}	D_{13}		S_{31}^{*}	D_{33}	D_{35}^{***}		
Saclay 76	2280			2001		1894		
CMU-LBL76		1920		2070	2070	1925		
CMU-LBL78		1830		2150	2010	1930		
K-H 78	1880			1908		1901		
[70,1-]	S_{11}^{****}	D_{13}^{****}	S_{11}^{****}	D_{13}^{***}	D_{15}^{****}		S_{31}^{****}	D_{33}^{****}
Saclay 76	1519	1525	1673	1710	1660		1623	1723
CMU-LBL76	1550	1520	1624	1661	1678		1634	1695
CMU-LBL78	1540	1525	1640	1670	1680		1620	1730
K-H 78	1526	1519	1670	1731	1679		1610	1680
[70,3-]	D_{15}	G_{17}^{***}	D_{13}^{**}	D_{15}^{**}	G_{17}	G_{19}^{***}	D_{35}	G_{37}
Saclay 76		2141	2029	2076		2133		
CMU-LBL76		1995	2065	2300	2191	2220	2300	2200
CMU-LBL78		(1990)	2100		2200	(2200)		
K-H 78		2140	2081	2228		2268	2305	2215
[70,5-]	G_{19}	I_{111}	G_{17}	G_{19}	I_{111}^{***}	I_{113}	G_{39}	I_{311}
K-H 78				2792	2577		2468	
[70,7-]	I_{113}	L_{115}	I_{111}	I_{113}	L_{115}	L_{117}	I_{313}	L_{315}
K-H 78								2794
[70,0+]	P_{11}		P_{13}				P_{31}^{*}	
CMU-LBL76	1710		(1800)				1600	
[70,2+]	P_{13}	F_{15}	P_{11}^{***}	P_{13}	F_{15}^{**}	F_{17}	P_{33}	F_{35}
Saclay 76			1729		2025			
CMU-LBL76			(1810)		(1965)			
CMU-LBL78		(1770)	(1710)		1970			
K-H 78			1723		1882			

resonances are the candidates for [56, 1^-] multiplets. There are some other candidates for [70, 0^+] and [70, 2^+] multiplets. The SU(6) × O(3) classification of nucleon resonances from references 2), 3) and 4) is listed in Table I–2).

As is well known, the pion-nucleon elastic scattering amplitudes are decomposed into the *s*-channel iso-spin amplitudes as the following formula,

$$A(\pi^+p\to\pi^+p)=A^{3/2}$$
$$A(\pi^-p\to\pi^-p)=1/3(A^{3/2}+2A^{1/2})$$
$$A(\pi^-p\to\pi^\circ n)=\sqrt{2}/3(A^{3/2}-A^{1/2}),$$

where $A^{1/2}$ and $A^{3/2}$ represent iso-spin 1/2 and 3/2 amplitudes, respectively. The charge exchange amplitude is expressed by the difference of $A^{1/2}$ and $A^{3/2}$ amplitudes.

In order to determine πN amplitudes completely, it is necessary to measure seven independent quantities because of the nucleon spin.

Since the pion-proton elastic scattering are easy one to study experimentally, there have been abundant data on the differential cross sections and polarization parameters of the $\pi^\pm p$ elastic scattering. Because of the difficulties in detecting neutral particles, $\pi^-p\to\pi^\circ n$ charge exchange scattering data are not so abundant comparing with those of the $\pi^\pm p$ elastic scattering. The early measurements on the differential cross sections and polarization parameters of the $\pi^-p\to\pi^\circ n$ scattering in the momentum region between 2.0 GeV/c and 3.0 GeV/c are listed in references 6)–13). So there still exist some ambiguities for phase shift analysis, because of a lack of the data on charge exchange scattering and spin rotation parameters R or A. Therefore, it is very important to study the $\pi^-p\to\pi^\circ n$ scattering besides the $\pi^\pm p$ elastic scattering.

In the high momentum region, the measurements on both the differential cross sections and the polarization parameters were performed at LBL[6),8)] and at Rutherford[7),9)], recently. The differential cross sections have been measured up to 2724 MeV/c and the polarization parameters have been measured up to 2267 MeV/c. These measurements were performed covering almost all angles with closely spacing incident momenta and with good precisions.

One of the objects of this experiment is to extend precise measurements of the differential cross sections and polarization parameters up to 3000 MeV/c and to provide new data for the partial wave analysis and to make a contribution to establish those high mass resonances mentioned above.

The present experiment has been performed as the first counter experiment at National Laboratory for High Energy Physics (KEK) using a pion beam from an internal target of the 8 GeV proton syncrotron.

This paper reports only the results of the measurements of the differential cross sections between 1969 MeV/c and 2965 MeV/c. The results of the measurements of the polarization parameters will be presented elsewhere[14),15)].

II. Beam

The negative pions produced at 10° from an internal beryllium target, 1.08 mmϕ × 20 mm, of KEK proton syncrotron, were transported to the experimental area through a two stage beam transport system consisting of four bending magnets and four quadrapole magnets. The beam transport system is shown in Fig. II–1. The first stage of the beam transport system brought the particles to an intermediate focus

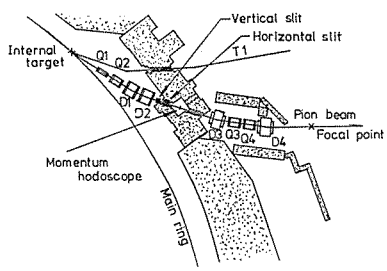

Fig. II–1. Layout of the beam transport system. D and Q denote a bending magnet and a quadrapole magnet, respectively.

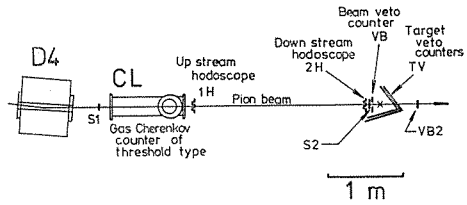

Fig. II–2. Arrangement of the beam definining counters. Counters S1, S2 are the scintillation counters. 1H and 2H are the scintillation hodoscopes. Counters VB, VB2 and TV's are veto counters. CL is a gas Cherenkov counter of threshold type.

with a momentum dispersion of 1% per cm. A lead collimator was placed at this point and limited the total momentum acceptance of the beam to be $\pm 0.5\%$ (FWHM). The second stage of the beam transport system focused the particles on a liquid hydrogen target.

The location of the counters used in the beam are shown in Fig. II–2. The counters S1 and S2 and the hodoscopes 1H were used as beam triggering counters. The upstream hodoscope 1H consisted of 6 vertical counters and 6 horizontal counters and the downstream hodoscope 2H consisted of 5 vertical counters and 4 horizontal counters. These counters were arranged so as to give the spacial resolution of 7 mm and 5 mm for the hodoscopes 1H and 2H, respectively. The hodoscopes 1H and 2H were used to measure the trajectories of the incident pions. The counter VB having a hole of 18 mm (vertical) $\times$ 26 mm (horizontal) was placed in front of the target to define the cross section of the beam.

The beam size was 17 mm (FWHM) in horizontal direction and 14 mm in vertical direction at the target point. The beam contained about $0.5 \sim 0.8\%$ and $0.8 \sim 1.5\%$ of negative muons and electrons depending on the momentum, respectively. The contamination of muons and electrons were reduced to be negligibly small by the use of the gas Cherenkov counter of threshold type placed behind the counter S1.

The beam spill were 300 msec long with 1/2 cycle and contained $2 \sim 5 \times 10^5$ pions per 10^{12} circulating protons of 8 GeV.

The momentum of the beam was calibrated using the time of flight for pions and protons besides the field measurement of the magnets of the beam transport system. The systematic uncertainty of the beam momentum is estimated to be 0.5%.

III. Experimental Apparatus

A plan view of the experimental set up is shown in Fig. III–1. The π° mesons produced at the target were detected by the π° detection system placed one side of the beam. The π° detectors measured the directions and energies of the two γ-rays decaying from π° mesons. Thus the emission angles and momenta of the π° mesons were evaluated with a good precision.

The recoil neutrons were detected by an array of the plastic scintillators placed the other side of the beam. The information from the neutron detectors was mainly

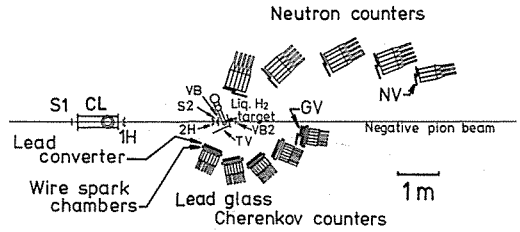

Fig. III–1. Plan view of the experimental set up.

used for the polarization measurements. In the differential cross section measurements, the neutron counters were used only to estimate backgrounds.

The veto counters surrounding the liquid hydrogen target were used to reject the charged particles leaving from the target.

III–1. The liquid hydrogen target

The liquid hydrogen target consisted of a vacuum chamber, a hydrogen condenser cooled down by a Cryodine refrigerator of model 1023 and a liquid hydrogen container connected to the condenser through a rather long horizontal heat pipe. Fig. III–2 shows the whole system of the target.

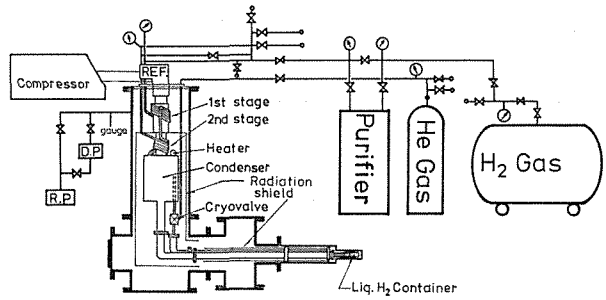

Fig. III–2. Schematic drawing of the liquid hydrogen target system.

The helium refrigerator, condenser and heat pipe were installed in a vacuum jacket and surrounded by the radiation shield. The cryovalve was provided to evacuate liquid hydrogen from the hydrogen container without warming up the target. The liquid hydrogen container was a cylinder of 50 mmϕ, 30 mm high made of Mylar sheets. Mylar sheets of 250 μm were used for top and bottom caps of the liquid hydrogen container and 125 μm for a side wall.

The heat pipe was made of a copper pipe. A meshed copper pipe was inserted in this pipe for making use of capillary action of liquid hydrogen to realize quick transfer of liquid hydrogen from the condenser to the liquid hydrogen container.

The vacuum jacket around the liquid hydrogen container was made of 1.5 mm aluminum and the Mylar windows of 250 μm were provided at the beam path. Materials encountered by the γ-rays emitted from the target were a Mylar sheet of 125 μm and aluminum of 1.5 mm.

III–2. Target veto counters

As is shown in Fig. III–3, the liquid hydrogen target was surrounded with as-

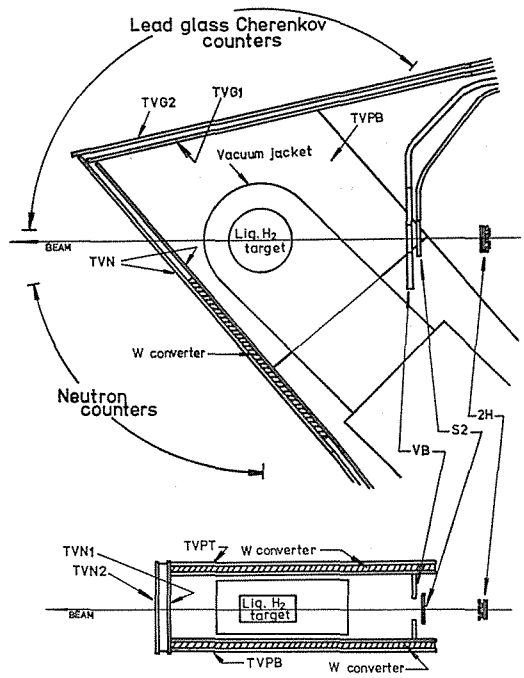

Fig. III–3. Target veto counters. Tungsten plates of 3 mm placed between counters TVPT, TVPB and TVN and acted as converters of γ-rays.

sembly of anti-counters of TVPT, TVPB, TVG1, TVG2, TVN and VB2 detecting all charged particles leaving the target except those that scattered back toward the direction of the heat pipe.

Tungsten plates of 3 mm placed between those anti-counters acted as converters of γ-rays leaving the target for directions other than toward the array of the π° detectors. The same anti-counters were used for the measurements of the polarization parameters. More details are described by M. Minowa[14].

III–3. π° detectors

The π° detection system consisted of five boxes of the π° detectors. Each box of the π° detection system consisted of 1.43 X_0 lead converter, four layers of multiwire spark chambers and 5×6 or 6×6 lead glass Cherenkov counters assembled in a square. All together, 174 lead glass Cherenkov counters were used in the experiment. Fig. III–4 shows the schematic view of the π° detector. The γ-rays decaying from π° mesons were converted into an electron-positron pair in the lead converter and trajectories of showers were recorded with the multiwire spark chambers and then totally absorbed in the lead glass Cherenkov counters.

The π° detection system was set up one side of the beam to cover the angles from 4° to 135° in the laboratory system. The angles between the two γ-rays decaying from π° mesons become smaller as the momentum of π° mesons increase. Therefore, the distance of each box was chosen to detect the two γ-rays from π° mesons with at least every other lead glass counters. The set up parameters of the π° detectors are listed in Table III–1.

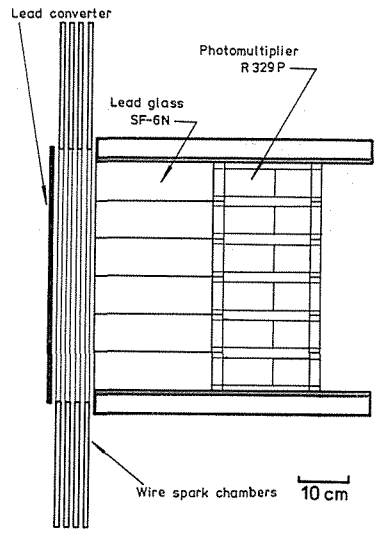

Fig. III–4. Construction of the π^0 detector. Each box of the π^0 detection system consisted of a lead converter of $1.43X_0$, four layers of multiwire spark chambers with which trajectories of showers were recorded, and 5×6 or 6×6 lead glass Cherenkov counters assembled in a square in which showers were totally absorbed.

Table III–1. Set up parameters of the boxes of the lead glass Cherenkov counters.

Box number	Construction the counter	Distance from the target	Angle of the center of the counter Box	Angular range covered by the counter block (Lab. frame)
Box #1	6×5	227.4 cm	9.0 deg	4.28– 13.72 deg
Box #2	6×6	154.1 cm	27.0 deg	18.69– 35.30 deg
Box #3	6×6	125.9 cm	51.0 deg	40.83– 61.09 deg
Box #4	6×6	99.0 cm	80.6 deg	67.75– 93.35 deg
Box #5	6×6	78.2 cm	117.1 deg	101.05–133.15 deg

a) Multiwire spark chambers

Each chamber had the same effective area of 50×50 cm^2. The frames of the chambers were made of epoxy glass (G–10) of 10 mm thick. A schematic view of the chamber is shown in Fig. III–5. Wire planes were made of 100 μm copper wires having spacing of 1 mm with the tension of 100 gw. The windows of the chambers were made of Mylar sheets and Acler sheets of 75 μm and 25 μm, respectively. The magnetostrictive readout system[16] was used and was able to readout up to seven tracks.

In order to minimize the dead space of the π^0 detectors, the width of the chamber frames were designed as narrow as possible. The magnetostrictive lines were embodied into the chamber frames so as to place other chambers closely.

Wires of two planes having a gap of 10 mm were arranged in parallel[17] so as to obtain the maximum efficiency for the multitrack events caused by electro-magnetic showers initiated by γ-rays. Four chambers were set in front of each box of the lead glass Cherenkov counters, and could read four coordinates, X, Y, U and V. The U and V coordinates were inclined $\pm15°$ with respect to the Y coordinate.

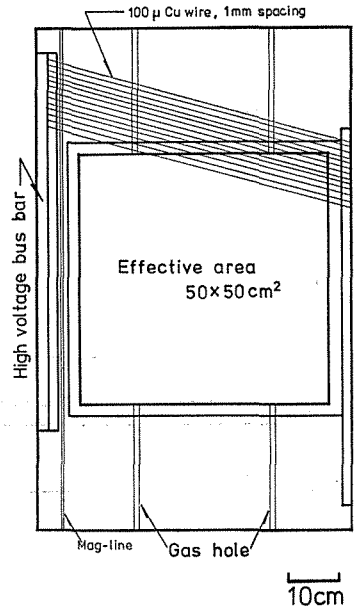

Fig. III–5. Schematic view of a multiwire spark chamber. Each chamber had the same effective area of 50×50 cm^2. The frames of the chambers were made of epoxy glass of 10 mm thick.

The high voltage pulses were applied to the chamber from a charge line of 21Ω through Thyratron (CX 1154 or CX 1157). The recovery time of the pulsing system was about 30 msec. The pulse width and pulse height were 200 nsec and 6 KV, respectively. A mixture of helium and neon was flowed to each chamber with a speed of 80 cc/min. The electronic block diagram of the multiwire spark chamber system is shown in Fig. III–6. Trigger pulses were first sent to the Krytrons which generated high voltage trigger pulses for the Thyratron. The chambers were fired 300 nsec after the master triggers.

The efficiency for multitrack events was measured using a multitrack generator[18]. The system generated up to three tracks by electrons from a ^{90}Sr source. An efficiency of 95% for three tracks events was achieved.

The electro-magnetic showers developed in the lead converters of 8 mm and the multiple Coulomb scattering results the spacial spread of the electron tracks in the multiwire spark chambers. Therefore, the accuracy in determining conversion points of γ-rays with the π° detection system was measured as a function of thickness of lead converters by using electron beams at Institute for Nuclear Study, 1.3 GeV electron syncrotron. The spacial resolution of multiwire spark chambers for γ-rays was about ± 13 mm on an average and was in good agreement with the Monte Carlo calculations by D. F. Crawford and H. Messel[19].

Finally, the efficiency of multiwire spark chambers including the γ-conversion efficiency amounted to 60% on an average.

b) Lead glass Cherenkov counters

A unit of lead glass Cherenkov counter was made of SF–6N lead glass[20], having a cross section of 7.5×7.5 cm^2 and a length of 23.5 cm (13.9 X°). The density and

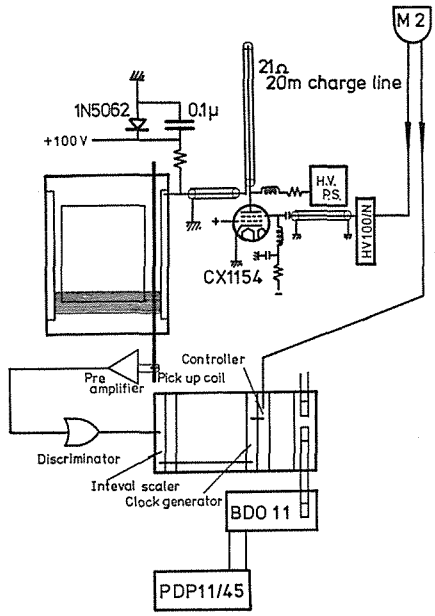

Fig. III–6. Block diagram of the pulsing system of the multiwire spark chamber system.

A wire chamber controller module generated a interrupt signal to PDP11/45 computer, a inhibit pulse to interval scaler modules and a start signal to a clock generator module. A clock generator module generated 50 Mhz serial pulses to interval scaler modules. A interval scaler modules stored the number of clocks corresponding to a interval of the front fiducial signal and a spark signal.

radiation length of SF–6N lead glass are 5.20 g/cm^3 and 1.69 cm, respectively. Each unit of a lead glass was viewed by the photomultiplier of R329P manufactured by HAMAMATSU TV-Co. Ltd.

The gain and the energy resolution of each lead glass counter were measured from 500 MeV to 2500 MeV by using the electrons contained in the pion beam. For this calibrations the internal target of beryllium was replaced by a tungsten target to increase the electrons in the pion beam. The calibrations were executed at the beginning of the machine time after the long shut down. The variation of gains within a short period was monitored by means of a light emission diode embodied into each counter.

The energy resolution was expressed as $\Delta E/E=\alpha\sqrt{E(\mathrm{MeV})}$ and the value for α was 5.42 on an average. The typical energy scale and energy resolution were shown in Fig. III–7–a) and b). The energy losses of electrons in lead converters of 8 mm and 10 mm thick were measured at 500 MeV, 1000 MeV and 1500 MeV.

The pulse height dependence on the position and direction of electrons for single lead glass Cherenkov counter was measured. At the same time the energies deposited in the adjacent counters were also measured. These dependences were taken into account to the analysis of events.

The biases of each lead glass Cherenkov counter were set at 200 MeV for the forward two boxes and 100 MeV for others.

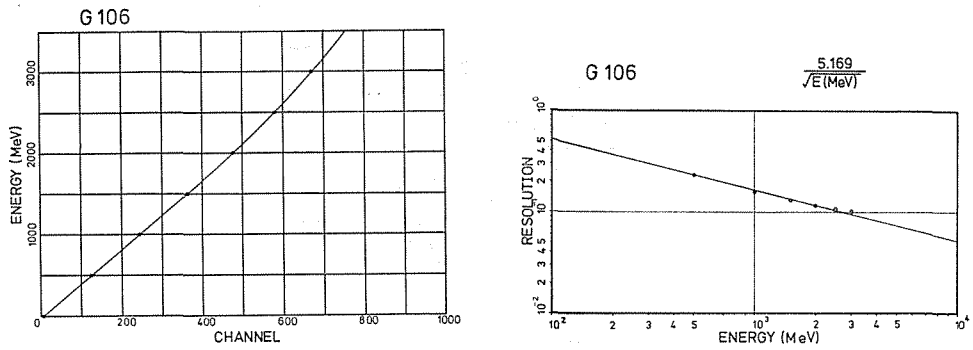

(a) (b)

Fig. III–7–a). Linearity of a lead glass Cherenkov counter. Small circles represent the measured points and a solid line is obtained from least-squares fit of these measured points.

Fig. III–7–b). Energy resolution of a lead glass Cherenkov counter. A horizontal axis indicates a incident electron energy and a vertical axis indicates a resolution of lead glass Cherenkov counter, $\Delta E/E$. Small circles indicate measured points . A solid line is obtained from a parameter fit of α.

III–4. Neutron counters

The neutron detection system consisted of five boxes of 118 neutron counters made of plastic scintillators. Each box was assembled in square with 5×3 or 5×4 or 5×5 counters. The dimension of plastic scintillator was 10 cm wide, 10 cm high and 30 cm long. The anti-counters were placed in front of each box of neutron counters.

The details of constructions and performances are described elsewhere[14].

III–5. Electronics

A block diagram of electronics is shown in Fig. III–8. Master signals were generated when the following conditions were satisfied.

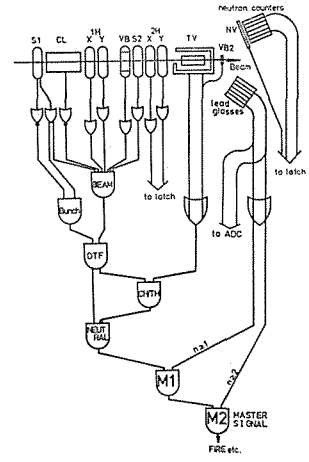

Fig. III–8. Block diagram of the fast electronics.

1) pion beam passed through the beam trigger counters,
2) pion beam did not bunch,
3) no charged particle was emitted from the target,
4) no extra γ-ray was emitted,
5) more than two lead glasses were fired.

The master signals performed a variety of functions,

1) to fire the wire spark chambers,
2) to open the gates for CAMAC modules,
3) to generate an inhibit signal of 30 msec long and
4) to generate the interrupt signal to the PDP11/45 computer.

The details of the electronics is described elsewhere[14].

III–6. On-line

The magnetostrictive readout system for the multiwire spark chambers was used to read the position of γ-showers created in the lead converter. In order to provide the data storage time of the interval scalers of the readout system, the interrupt signals for the PDP11/45 computer were generated by the wire spark chamber controller 500 μsec after a master trigger.

The PDP11/45 computer stored the following information; pulse heights of the lead glass Cherenkov counters, the addresses of the neutron hodoscopes and the beam hodoscopes and locations of γ-showers in the multiwire spark chambers and counting numbers in many blind scalers.

Each event required the memories of 864 bytes. These data were stored within about 6 msec. The event rate was about 6 for target full runs and 2 for empty on an average for each beam spill time. The inhibit time was chosen to be 30 msec taking into account the recovery time of the power supply of the Thyratron.

The data stored in the core memories in the PDP11/45 computer were transcribed to 9-track magnetic tapes at the end of the beam spill. At the same time the data were also transmitted to the central computer HITAC 8800 through KEKNET[21].

The hardware configulation concerning with the on-line system are shown in Fig. III–9. The PDP11/45 computer displayed features of the raw data on the

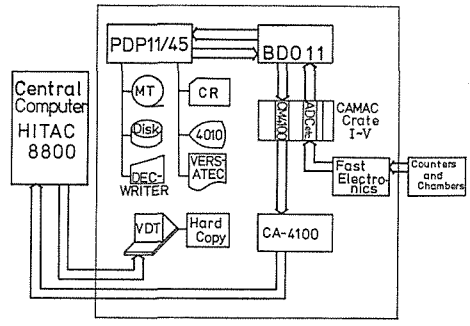

Fig. III–9. Hardware configuration of the on-line system. CAMAC system was used for the data taking system. Five crates were connected to PDP11/45 computer through the branch driver of BDO11. PDP11/45 computer was also linked to the central computer HITAC 8800 through the CAMAC system. The results processed by the central computer HITAC 8800 were returned to the video terminal in the counting room.

storage scope TEKTRONIX 4010, such as the histogram of the number of event of the lead glass Cherenkov counters, two dimensional display of the γ-showers on the multiwire spark chambers etc.

In the central computer HITAC 8800 the data were analyzed and reconstructed kinematically. The program for the central computer HITAC 8800 consisted of the two task. One received the data and analyzed them, and the other received the command and send back the results to a video terminal in the counting room. The kinematical quantities such as the effective mass and the opening angle of two γ-rays from π° meson and the momentum of π° meson were calculated for each event. Histograms of these quantities were accumulated. The efficiency of the multiwire spark chamber was also calculated. Some cuts were applied to these histograms and total amount of the candidates for charge exchange scattering event were estimated. The results of these calculations were sent back the video terminal in the counting room at the end of each run and at any time by typing the command to the PDP11/45 computer.

III–7. Data collection

The measurements on the differential cross sections were executed at July, 1977 and at November, 1977 and consumed about 320 hours. The beam intensity of the proton synchrotron varied from 5×10^{11} to 1×10^{12} protons per pulse during the measurements.

The differential cross sections have been measured at six incident pion momenta from 1969 MeV/c to 2965 MeV/c, in the angular range between $\cos\theta^*=-0.95$ and $\cos\theta^*=+0.95$.

The measurement with the liquid hydrogen target and the empty target had been repeated for every 10 hours. About 30 to 40% of the machine time was spent for the measurement with the empty target.

Because of the large forward differential cross section, enough numbers of events for forward angles were collected within a short period when all five boxes of the π° detection system were fired. The triggering rate of the π° detection system were more than 5 events for single beam spill, and the total duration of the dead time due to the read out time and the recovery time of the high voltage pulsing circuits of the spark chamber, exceeded more than 50% of the beam spill time. Therefore, about 50 to 70% of the data collection time was consumed without the most forward box of the lead glass Cherenkov counters at each momentum except 1969 MeV/c.

The total amount of $5\sim6\times10^9$ π^-'s were used for the measurements with the target filled with liquid hydrogen and $3\sim4\times10^9$ π^-'s with the empty target at each momentum. Total events amounted to from 120×10^3 to 200×10^3 and from 50×10^3 to 70×10^3 with the target full and empty, respectively. The numbers of events collected by this measurement are listed in Table IV–1.

IV. Data Reduction and Analysis

The general procedure of the data analysis was as follows;

1) selection of the two γ-rays events,
2) reduction of the energies and directions of the two γ-rays,
3) selection of the effective mass of two γ-rays and the reconstruction of the π° momentum,
4) event selection with respect to the kinematical quantities,

5) background subtraction,
6) Monte Carlo simulation of the acceptance of the π° detection system and
7) reduction of the differential cross sections.

IV–1. Events of the two γ-rays

The events caused by two γ-rays were selected at the first step of the data analysis. According to the triggering conditions described in Chapter III–5, more than two lead glass Cherenkov counters were required to be fired. About 70% of events were triggered by adjacent two lead glass Cherenkov counters. However, the π° detectors were carefully set up, so that even at the forward angles, two γ-rays from π° mesons must hit at least every other or more separated two lead glass counters. Therefore, the events triggered by adjacent two lead glass Cherenkov counters were caused by a single γ-ray. The events which fired at least every other or more separated two lead glass Cherenkov counters were selected as the two γ-rays events. However, among these two γ-rays events, about 10% of γ-rays were detected with two or more adjacent lead glass counters. These events were also selected as the two γ-rays events.

Finally the two γ-rays events amounted from 20% to 30% of the all trigger events. The three γ-rays events were less than 1% of the two γ-rays events. The numbers of the trigger events and the two γ-rays events are listed in Table IV–1 together with the total number of incident π^- mesons.

Table IV–1. Total amount of the beam and trigger events.

Momentum	1969 MeV/c		2172 MeV/c		2370 MeV/c	
F: target full E: target empty	F	E	F	E	F	E
Beam ($\times 10^6$)	5445	2968	5403	2699	5744	3006
Trigger	190458	51477	118806	47205	123291	49864
Two gamma rays	36905	8924	28616	6438	31284	7540
Mass cut	30979	7334	23928	5124	26141	5896
$P^{cm}_{\pi^\circ}$ cut	23456	4883	16639	3020	17083	3244

Momentum	2569 MeV/c		2767 MeV/c		2965 MeV/c	
F: target full E: target empty	F	E	F	E	F	E
Beam ($\times 10^6$)	6093	4103	5771	3264	5994	3818
Trigger	157455	73104	122557	52263	149890	55808
Two gamma rays	34706	10586	33512	8168	32038	10361
Mass cut	28632	8249	27780	6414	26465	8047
$P^{cm}_{\pi^\circ}$ cut	18233	4413	16708	3201	15593	4147

The events number after the selections are also listed.

IV–2. Reduction of the energies and directions of the γ-rays

The energies of γ-rays were evaluated from the pulse height of lead glass Cherenkov counters. According to the results of the energy calibration measurements described in Chapter III–3–b), the most of the energy of γ-rays is deposited in a single lead glass Cherenkov counter and a few percent of the energy is deposited in neighbouring counters. Therefore, the energies deposited in neighbouring counters were added together to evaluate the energy of γ-rays. The energy loss in the lead

converter placed in front of the lead glass Cherenkov counter was estimated from the measured energy loss of electrons and the results of the Monte Carlo calculation of the electron and photon initiated electro-magnetic showers in lead by D. F. Crawford and H. Messel[19]. Since the efficiency of finding the tracks of γ-showers in the wire spark chambers was about 60% for a single γ-ray, the tracks of the γ-showers associated with both two γ-rays from π° mesons were recorded only at a rate of 30 to 40% of the two γ-rays events. For these events the direction of γ-rays were determined precisely with the spacial resolution of ± 13 mm in the wire spark chambers. However, for the rest of events only one of γ-rays or none of γ-rays was recorded in the wire spark chamber. The γ-rays whose shower tracks were not recorded in the wire spark chambers were assumed to hit the center of the lead glass Cherenkov counter. In the case of adjacent two or more lead glasses were fired, the mean of the centers of these lead glass counters weighted by their pulse height was adopted as the hit position of the γ-ray. The direction of the γ-rays were evaluated for each γ-rays by assuming the γ-rays were produced at the center of the liquid hydrogen target. The effective mass of the two γ-rays, μ, was calculated by the following relation;

$$\mu^2 = 2k_1k_2(1-\cos\phi),$$

where k_1 and k_2 are the energies of two γ-rays and ϕ is their correlation angle.

The distribution of the effective mass for all events after the subtraction of the backgrounds measured with the empty target runs is shown in Fig. IV–1–a) for the 2370 MeV/c runs. The FWHM (full width at half maximum) of the mass distribution is about 40 MeV/c^2. Fig. IV–1–b) shows the mass distribution for the events in which shower tracks of both γ-rays were recorded in the wire spark chambers. The FWHM of the mass distribution for these events are clearly narrower than that for all events and amounts to be about 35 MeV/c^2.

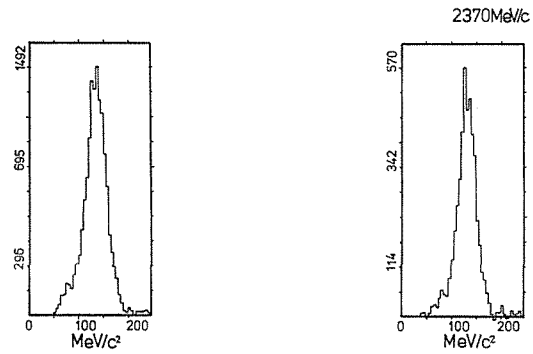

(a) (b)

Fig. IV–1–a). Distribution of the effective mass of two γ-rays for all events collected at 2370 MeV/c. The target empty events were subtracted.

Fig. IV–1–b). Distribution of the effective mass for the events in which shower tracks of both γ-rays were recorded in the wire spark chambers.

IV–3. Reconstruction of the π° momentum

In the present experiment, the energies of γ-rays from π° mesons (k_1 and k_2) were measured with the lead glass Cherenkov counter having the energy resolution described in Chapter III–3–b). The energy resolutions of the lead glass Cherenkov

counters were rather poor and amounted to be 17% on an average at 1 GeV. On the other hand, the correlation angles of the two γ-rays were measured with a fairly good precision, but still there are some uncertainties. Therefore, the energies and correlated angles of two γ-rays from π° mesons, k_1^r, k_2^r and ϕ^r which give the minimum value for the following quantity χ^2, were evaluated for each events,

$$\chi^2=\frac{(k_1-k_2^r)^2}{\sigma_1^2}+\frac{(k_2-k_2^r)^2}{\sigma_2^2}+\frac{(A-A^r)^2}{\sigma_A^2}$$

with $A=\mu^2/2(1-\cos\phi)$ where μ denotes the mass of π° mesons. The quantities σ_1 and σ_2 are the energy resolution of the lead glass Cherenkov counters, respectively. The quantities σ_A is a constant related to the spacial resolution of the γ-shower tracks recorded in the wire spark chambers or the lead glass Cherenkov counter. k_1, k_2 and ϕ are the measured values for the energies and correlation angles of two γ-rays from π° mesons. In this calculation the following kinematical constraint was required for k_1^r, k_r^r and ϕ^r,

$$k_1^r\cdot k_2^r=\frac{\mu^2}{2(1-\cos\phi^r)}\,.$$

By using thus obtained k_1^r, k_2^r and ϕ^r, the momentum of π° mesons were evaluated for each events.

Fig. IV–2–a) shows the momentum distribution of the π° mesons in the center of mass system for the 2370 MeV/c runs. The resolution for the momentum was found to be $\pm 8\%$ on an average for all events. For the events in which both γ-showers were recorded with multiwire spark chambers the resolution was found to be $\pm 5\%$ on an average and is shown in Fig. IV–2–b). Low momentum events in the momentum distribution were mostly due to the inelastic reactions such as the $\pi^-p\to\pi^\circ\pi^\circ n$ reaction in this measurement.

The events having the effective mass from 75 MeV/c^2 to 195 MeV/c^2 were selected. The events due to the $\pi^-p\to\eta n$ reaction were completely removed by this selection. About 14% of the two γ-rays events were rejected on an average.

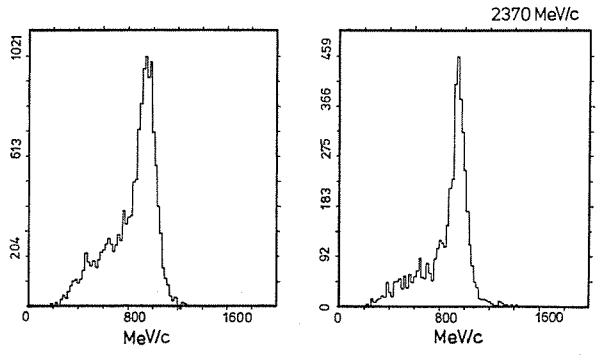

(a) (b)

Fig. IV–2–a). Momentum distribution of the π° mesons in the center of mass system for all events at 2370 MeV/c. The events with the target empty were subtracted.

Fig. IV–2–b). Momentum distribution of the π° mesons in the center of mass system at 2370 MeV/c for the events in which both γ-showers were recorded with wire spark chambers.

At the second step, the events having the center of mass momentum from $0.76 \times p_{\pi^\circ}^{nom}$ to $1.21 \times p_{\pi^\circ}^{nom}$ were selected on an average. The quantity $p_{\pi^\circ}^{nom}$ is the nominal momentum of π° mesons in the center of mass system. This selection reduced the background due to the inelastic process. The numbers of the selected events are also listed in Table IV–2.

Table IV–2. The numbers of the selected events.

Momentum	1969 MeV/c	2965 MeV/c
Beam	5445 ($\times 10^6$)	5993 ($\times 10^6$)
Trigger	96274	67727
Two gamma rays	20633 (21%)	16559 (24%)
Mass cut	17586 (18%)	14395 (21%)
$P_{\pi^\circ}^{cm}$ cut	14554 (15%)	9402 (14%)

The backgrounds measured with the empty target was subtracted. A percentage indicates the ratio to the trigger events.

The distributions of the correlation angle of two γ-rays before and after of those selections were plotted in Fig. IV–3–a)–b) and show that the events having large correlation angles were reduced by the mass and momentum selections.

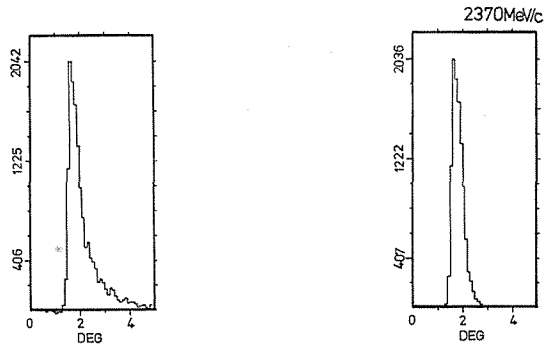

(a) (b)

Fig. IV–3–a). Distribution of the correlation angle of two γ-rays before the selections.
Fig. IV–3–b). Distribution of the correlation angle of two γ-rays for the selected events.

IV–4. Background subtraction

a) Background from material other than hydrogen in the target

The reaction point could not be determined in the present measurement. The background events from materials other than hydrogen in the target must be subtracted experimentally. The events measured with the target empty were subtracted after applying the same selection of events. The background due to this origin amounted from 33 to 38% depending on the beam momentum. The number of the selected events with the target empty are also listed in Table IV–1.

Fig. IV–4 shows the momentum distribution of π° mesons for the target empty runs together with that for the target filled with hydrogen at 2370 MeV/c. The sharp peak corresponding to the charge exchange scattering is not seen in the momentum distribution for the target empty.

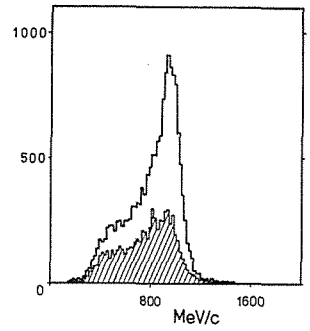

Fig. IV–4. Momentum distributions of π° mesons for the target filled with hydrogen together with that for the target empty runs at 2370 MeV/c. The events for the target empty runs are indicated by inclined lines and are normalized to the target filled events according to the numbers of the incident particles.

b) Background from the inelastic processes

The events due to the $\pi^-p\to\eta n$ reaction was clearly separated in the distribution of the effective mass of the two γ-rays, and rejected by the effective mass selection. The effective mass distribution at 2370 MeV/c is shown in Fig. IV–5 as an example. The η events were about 10% of the π° events at this momentum.

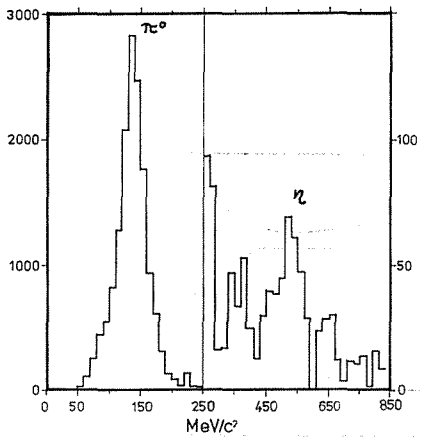

Fig. IV–5

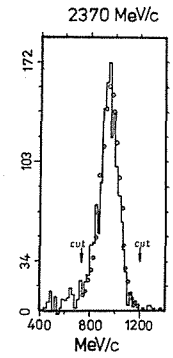

Fig. IV–6

Fig. IV–5. Effective mass distribution of two γ-rays up to the high mass region at 2965 MeV/c. A η peak can be seen around 550 MeV/c^2.

Fig. IV–6. Momentum distribution of π° mesons in the center of mass system for neutron coincidence event. The open circles indicate the results of the Monte Carlo simulation.

Among the inelastic processes, the $\pi^-p\to\pi^\circ\pi^\circ n$ reaction was the main source of the background on the present measurement. The π° mesons emitted from this reaction possesses lower momentum than the π° mesons from the charge exchange scattering. Therefore, a large portion of events due to the inelastic process were rejected by the selection with the center of mass momentum.

These inelastic π° mesons possess the highest momentum when it is caused through the $\pi^-p\to\pi^\circ\Delta$ channel. This momentum are about 15% less than the nominal mo-

mentum for the charge exchange scattering. However, still some portion of the background due to this origin was expect to remain in the selected events after the selection with the center of mass momentum. For about 20% of the selected events, the recoiled neutron was detected by satisfying the kinematics of the charge exchange scattering. As is seen in Fig. IV–6, the distribution of the center of mass momentum of these neutron coincidence events shows no tails in the low momentum side and coincides with the Monte Carlo results which do not include the inelastic process. Therefore, the background due to the inelastic process was estimated with the following procedure.

At first after the subtraction of the target empty events was made, the angular region was divided into nine. In each angular region the momentum distribution of the selected events was compared with the Monte Carlo distribution. The background mainly contained at the lower side of the peak was evaluated. Thus the angular dependence of the background was evaluated.

On the other hand, the momentum distribution of all selected events was compared with the momentum distribution of the neutron coincidence events. The total number of background was obtained with this comparison. A sum of backgrounds evaluated at each angular region was normalized to this total number of background. An angular distribution of the inelastic background thus obtained are shown in Fig. IV–7.

These angular distributions were approximated with polynomial functions of 3rd and 2nd order with respect to the beam momenta and $\cos\theta$, respectively. The background of this origin amounted to about 7 to 12% depending on the beam momentum.

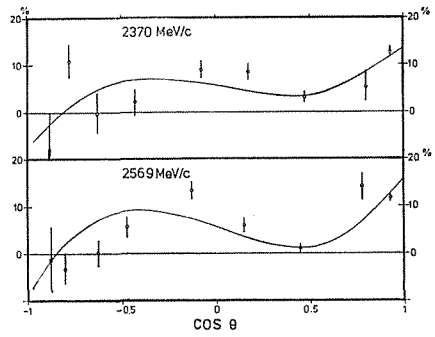

Fig. IV–7. Angular distribution of the inelastic background at 2370 MeV/c and 2569 MeV/c. The curves indicate the fitted polynomial functions of 3rd and 2nd order with respect to the beam momenta and $\cos\theta$, respectively.

IV–5. Monte Carlo simulation

The Monte Carlo simulation were performed to evaluate the detection efficiency and angular resolution of the present measurement.

At the first step, the events were generated assuming the uniform angular distribution for π° mesons. Then the detection efficiencies of the detectors were calculated. The energy resolutions of the lead glass Cherenkov counters, the conversion efficiency of the lead converter and the efficiency of the wire spark chamber and so

on, were folded into the calculation. The events selections were performed as same as the data reduction procedure for the measured events. Using the detection efficiency thus calculated, the preliminary values of the differential cross sections were evaluated. Then the second stage Monte Carlo simulations were performed by using the angular distribution of π° mesons thus obtained. The detection efficiencies calculated with these Monte Carlo simulations for the 2370 MeV/c run are shown in Fig. IV–8. The results of the first and second simulation were well coincided within the accuracy of the calculation. The results of the second Monte Carlo simulation were used to evaluate the differential cross sections and the background, and were also used to test the features of the various distribution of kinematical quantities as was described in the previous chapter.

The detection efficiencies certainly possess peaks and dips corresponding to gaps between the five boxes of the π° detectors.

The angular resolutions of the detection system were also evaluated with the Monte Carlo simulation and are shown in Fig. IV–9. As is seen in the figure, the angular resolution $\Delta \cos\theta^*_{\pi^\circ}$ were smaller than 0.05. The angular bin width of the differential cross sections was chosen to be 0.05.

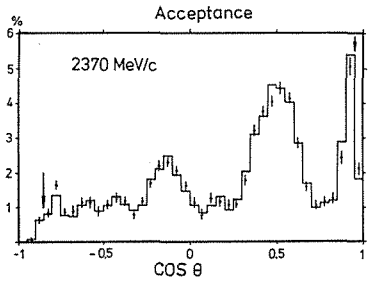

Fig. IV–8

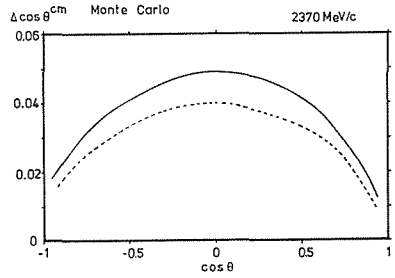

Fig. IV–9

Fig. IV–8. Detection efficiency calculated by the Monte Carlo simulation at 2370 MeV/c. The open circles indicate the results of the first Monte Carlo simulation with the assumption of the uniform angular distribution for π° mesons. A histogram indicates the results of the second Monte Carlo simulation by using the angular distribution of π° mesons which obtained from the first Monte Carlo simulation.

Fig. IV–9. Angular resolutions of the detection system at 2370 MeV/c evaluated with the Monte Carlo simulations. The solid and dashed curves indicate the angular resolutions for all events and events in which tracks of γ-showers were recorded in the wire spark chambers, respectively.

IV–6. Reduction of the differential cross section

The differential cross sections were calculated by the following formula,

$$\frac{d\sigma}{d\Omega} = \frac{Y}{N_b \cdot n_t \cdot l_t \cdot \Delta \cos\theta \cdot 2\pi \cdot \eta_m},$$

with

Y; yields,
n_t; density of target protons,
N_b; number of incident pions,
l_t; effective length of the target,

η_m; detection efficiency calculated by the Monte Carlo simulation,
$\Delta \cos\theta$; bin width.

Since the liquid hydrogen container of the target was a cylindrical shape, the effective length of the target was evaluated taking into account the spread of the incident beam. The intensity distribution of the incident pions across the beam at the target position were estimated by using the information from the hodoscope 2H placed in front of the liquid hydrogen target. Then the effective length of the target was calculated with the horizontal distribution of the incident beam thus obtained.

The beam divergence was estimated by using the information from the hodoscopes 1H and 2H and amounted to 15 mrad on an average. The correction to the target length due to the beam divergence was estimated to be less than 0.1% and was neglected.

IV–7. Correction to the normarization

a) γ-ray conversion in liquid hydrogen and the surrounding materials

A small portion of γ-rays from π° mesons were converted by the materials surrounding the liquid hydrogen target, before they transversed anti-counters. These events were rejected by the anti-counters. The materials responsible to this conversion of γ-rays were hydrogen, a Maylar container, an aluminum target jacket of 1.5 mm thick and the plastic scintillator of anti-counters. The total correction due to this origin was approximately 4.7% for two γ-events.

b) Accidental coincidence and anti-coincidence

The rate of accidental coincidence between the beam counters S1, 1HX, 1HY and S2 was negligibly small. The rate of accidental coincidence between the beam and the lead glass Cherenkov counters was also negligibly small because of low counting rates of the lead glass Cherenkov counters. The accidental rate between the beam counters and anti-counters surrounding the hydrogen target ranged from 0.6% to 1.8% depending on the beam intensity.

c) Electrons and muons contamination in the beam

The electrons and the muons in the beam were almost removed by use of the gas Cherenkov counter of threshold type. The electrons and muons contamination due to the inefficiency of the gas Cherenkov counter was found to be less than 0.1%.

The muon contamination due to $\pi^- \to \mu^- \bar{\nu}$ decay at the down stream of the gas Cherenkov counter was calculated to be 0.8% of the pion beam on an average.

d) Branching ratio for $\pi^\circ \to 2\gamma$

The branching ratio of 98.8% for the $\pi^\circ \to 2\gamma$ decay was taken into account for the correction.

e) Liquid hydrogen target

The liquid hydrogen target had been kept at a constant temperature during the measurement. However, bubbles were observed in liquid hydrogen. The density of bubbles were measured by taking photographs of the liquid hydrogen container. The correction due to this origin was found to be 0.4%.

V. Results and Conclusion

The results on the differential cross sections for charge exchange scattering are listed in Table V-1-a)-f). The errors presented in this table include only the statistical errors of the data, and those of the Monte Carlo simulations. The statistical errors of the Monte Carlo simulations were typically less than one third of the data. This ratio was kept almost the same at every data points, because the Monte Carlo simulations were performed with the number of generated events which were proportional

Table V-1-a). Experimental results of the differential cross sections.

Differential Cross Sections for the $\pi^-p\to\pi^0n$ Charge Exchange Scattering

Incident Pion Momentum	1969 MeV/c
(cos θ)	(mb/sr)
−0.825±0.025	0.022±0.008
−0.775±0.025	0.026±0.004
−0.725±0.025	0.038±0.006
−0.675±0.025	0.045±0.009
−0.625±0.025	0.034±0.007
−0.575±0.025	0.058±0.008
−0.525±0.025	0.036±0.006
−0.475±0.025	0.039±0.007
−0.425±0.025	0.054±0.008
−0.375±0.025	0.038±0.006
−0.325±0.025	0.056±0.006
−0.275±0.025	0.050±0.008
−0.225±0.025	0.044±0.007
−0.175±0.025	0.056±0.006
−0.125±0.025	0.078±0.006
−0.075±0.025	0.088±0.006
−0.025±0.025	0.102±0.007
0.025±0.025	0.098±0.007
0.075±0.025	0.089±0.007
0.125±0.025	0.074±0.008
0.175±0.025	0.107±0.008
0.225±0.025	0.091±0.007
0.275±0.025	0.090±0.007
0.325±0.025	0.057±0.007
0.375±0.025	0.053±0.005
0.425±0.025	0.037±0.004
0.475±0.025	0.030±0.003
0.525±0.025	0.024±0.003
0.575±0.025	0.019±0.003
0.625±0.025	0.019±0.003
0.675±0.025	0.032±0.004
0.725±0.025	0.049±0.007
0.775±0.025	0.091±0.010
0.825±0.025	0.126±0.010
0.875±0.025	0.183±0.012
0.925±0.025	0.311±0.010

Errors include only the statistical ones.

Table V-1-b). Experimental results of the differential cross sections.

Differential Cross Sections for the $\pi^-p\to\pi^0n$ Charge Exchange Scattering

Incident Pion Momentum	2172 MeV/c
(cos θ)	(mb/sr)
−0.825±0.025	0.029±0.006
−0.775±0.025	0.019±0.005
−0.725±0.025	0.028±0.005
−0.675±0.025	0.027±0.007
−0.625±0.025	0.030±0.006
−0.575±0.025	0.030±0.005
−0.525±0.025	0.029±0.005
−0.475±0.025	0.032±0.006
−0.425±0.025	0.036±0.005
−0.375±0.025	0.044±0.006
−0.325±0.025	0.037±0.006
−0.275±0.025	0.036±0.006
−0.225±0.025	0.030±0.005
−0.175±0.025	0.035±0.004
−0.125±0.025	0.046±0.005
−0.075±0.025	0.058±0.005
−0.025±0.025	0.068±0.006
0.025±0.025	0.042±0.005
0.075±0.025	0.068±0.007
0.125±0.025	0.078±0.008
0.175±0.025	0.084±0.007
0.225±0.025	0.084±0.007
0.275±0.025	0.073±0.008
0.325±0.025	0.076±0.006
0.375±0.025	0.058±0.005
0.425±0.025	0.051±0.004
0.475±0.025	0.045±0.003
0.525±0.025	0.040±0.003
0.575±0.025	0.035±0.003
0.625±0.025	0.025±0.003
0.675±0.025	0.032±0.003
0.725±0.025	0.027±0.006
0.775±0.025	0.064±0.011
0.825±0.025	0.095±0.013
0.875±0.025	0.144±0.015
0.925±0.025	0.245±0.012

Errors include only the statistical ones.

Table V–1–c). Experimental results of the differential cross sections.

Differential Cross Sections for the $\pi^- p \to \pi^0 n$ Charge Exchange Scattering

Incident Pion Momentum	2370 MeV/c
(cos θ)	(mb/sr)
−0.825±0.025	0.022±0.007
−0.775±0.025	0.024±0.004
−0.725±0.025	0.023±0.005
−0.675±0.025	0.020±0.005
−0.625±0.025	0.017±0.005
−0.575±0.025	0.013±0.004
−0.525±0.025	0.025±0.005
−0.475±0.025	0.023±0.004
−0.425±0.025	0.036±0.005
−0.375±0.025	0.031±0.005
−0.325±0.025	0.020±0.004
−0.275±0.025	0.016±0.005
−0.225±0.025	0.018±0.003
−0.175±0.025	0.014±0.003
−0.125±0.025	0.018±0.003
−0.075±0.025	0.018±0.004
−0.025±0.025	0.033±0.004
0.025±0.025	0.026±0.005
0.075±0.025	0.034±0.007
0.125±0.025	0.061±0.007
0.175±0.025	0.039±0.005
0.225±0.025	0.063±0.007
0.275±0.025	0.052±0.006
0.325±0.025	0.055±0.004
0.375±0.025	0.054±0.003
0.425±0.025	0.057±0.003
0.475±0.025	0.043±0.003
0.525±0.025	0.042±0.003
0.575±0.025	0.043±0.003
0.625±0.025	0.032±0.003
0.675±0.025	0.009±0.003
0.725±0.025	0.028±0.009
0.775±0.025	0.024±0.009
0.825±0.025	0.038±0.011
0.875±0.025	0.133±0.009
0.925±0.025	0.244±0.009

Errors include only the statistical ones.

Table V–1–d). Experimental results of the differential cross section.

Differential Cross Sections for the $\pi^- p \to \pi^0 n$ Charge Exchange Scattering

Incident Pion Momentum	2569 MeV/c
(cos θ)	(mb/sr)
−0.875±0.025	0.025±0.006
−0.825±0.025	0.015±0.004
−0.775±0.025	0.018±0.004
−0.725±0.025	0.009±0.004
−0.675±0.025	0.019±0.003
−0.625±0.025	0.020±0.003
−0.575±0.025	0.022±0.003
−0.525±0.025	0.023±0.004
−0.475±0.025	0.029±0.004
−0.425±0.025	0.022±0.003
−0.375±0.025	0.023±0.004
−0.325±0.025	0.010±0.003
−0.275±0.025	0.010±0.003
−0.225±0.025	0.009±0.002
−0.175±0.025	0.006±0.002
−0.125±0.025	0.011±0.002
−0.075±0.025	0.014±0.002
−0.025±0.025	0.019±0.003
0.025±0.025	0.025±0.005
0.075±0.025	0.047±0.006
0.125±0.025	0.039±0.006
0.175±0.025	0.044±0.005
0.225±0.025	0.041±0.005
0.275±0.025	0.052±0.004
0.325±0.025	0.048±0.003
0.375±0.025	0.056±0.003
0.425±0.025	0.053±0.003
0.425±0.025	0.045±0.003
0.525±0.025	0.042±0.003
0.575±0.025	0.035±0.003
0.625±0.025	0.025±0.003
0.675±0.025	0.012±0.003
0.725±0.025	0.017±0.005
0.775±0.025	0.016±0.006
0.825±0.025	0.039±0.008
0.875±0.025	0.127±0.007
0.925±0.025	0.231±0.007

Errors include only the statistical ones.

to the differential cross section.

The remaining systematic errors were due to

(i) background subtraction (±1%~2%),

(ii) effective length of the liquid hydrogen target (±0.3%),

(iii) rate of accidental coincidence (±0.05%~0.3%).

General features of the differential cross sections are characterized by the forward steep peak, the first dip around $\cos\theta^* = 0.7$ to 0.8, the second broad peak around $\cos\theta^* = 0.1$, the second dip around $\cos\theta^* = -0.2$, the third peak around $\cos\theta^* =$

Table V–1–e). Experimental results of the differential cross sections.

Differential Cross Sections for the $\pi^-p\to\pi^\circ n$ Charge Exchange Scattering

Incident Pion Momentum	2767 MeV/c
(cos θ)	(mb/sr)
−0.875±0.025	0.017±0.006
−0.825±0.025	0.015±0.004
−0.775±0.025	0.016±0.003
−0.725±0.025	0.013±0.003
−0.675±0.025	0.016±0.003
−0.625±0.025	0.017±0.003
−0.575±0.025	0.014±0.003
−0.525±0.025	0.014±0.003
−0.475±0.025	0.021±0.004
−0.425±0.025	0.020±0.004
−0.375±0.025	0.008±0.003
−0.325±0.025	0.007±0.002
−0.275±0.025	0.004±0.001
−0.225±0.025	0.007±0.002
−0.175±0.025	0.003±0.001
−0.125±0.025	0.004±0.002
−0.075±0.025	0.006±0.002
−0.025±0.025	0.009±0.002
0.025±0.025	0.017±0.004
0.075±0.025	0.012±0.004
0.125±0.025	0.026±0.005
0.175±0.025	0.021±0.006
0.225±0.025	0.030±0.004
0.275±0.025	0.040±0.003
0.325±0.025	0.038±0.003
0.375±0.025	0.047±0.003
0.425±0.025	0.053±0.003
0.475±0.025	0.044±0.003
0.525±0.025	0.039±0.003
0.575±0.025	0.036±0.003
0.625±0.025	0.013±0.002
0.675±0.025	0.008±0.004
0.725±0.025	0.015±0.009
0.775±0.025	0.019±0.006
0.825±0.025	0.021±0.006
0.875±0.025	0.124±0.006
0.925±0.025	0.208±0.006

Errors include only the statistical ones.

Table V–1–f). Experimental results of the differential cross sections.

Differential Cross Sections for the $\pi^-p\to\pi^\circ n$ Charge Exchange Scattering

Incident Pion Momentum	2965 MeV/c
(cos θ)	(mb/sr)
−0.925±0.025	0.020±0.011
−0.875±0.025	0.014±0.005
−0.825±0.025	0.013±0.003
−0.775±0.025	0.010±0.004
−0.725±0.025	0.006±0.002
−0.675±0.025	0.009±0.003
−0.625±0.025	0.008±0.002
−0.575±0.025	0.011±0.002
−0.525±0.025	0.015±0.003
−0.475±0.025	0.011±0.002
−0.425±0.025	0.009±0.003
−0.375±0.025	0.004±0.002
−0.325±0.025	0.007±0.001
−0.275±0.025	0.003±0.001
−0.225±0.025	0.004±0.001
−0.175±0.025	0.002±0.001
−0.125±0.025	0.004±0.001
−0.075±0.025	0.006±0.002
−0.025±0.025	0.006±0.002
0.025±0.025	0.009±0.003
0.075±0.025	0.011±0.004
0.125±0.025	0.014±0.004
0.175±0.025	0.011±0.003
0.225±0.025	0.022±0.003
0.275±0.025	0.019±0.002
0.325±0.025	0.029±0.002
0.375±0.025	0.037±0.003
0.425±0.025	0.028±0.002
0.475±0.025	0.036±0.002
0.525±0.025	0.032±0.002
0.575±0.025	0.029±0.003
0.625±0.025	0.013±0.003
0.675±0.025	0.007±0.005
0.725±0.025	0.027±0.009
0.775±0.025	0.014±0.007
0.825±0.025	0.024±0.004
0.875±0.025	0.079±0.004
0.925±0.025	0.168±0.005

Errors include only the statistical ones.

−0.5, the third diminutive dip and the backward peak smaller than the forward peak, as is seen in Fig. V–1–a)–f).

The slope of the forward peak becomes steep at higher momentum. The position of the first dip moves forward and the depth of the first dip increases as the beam momentum increases. However, the dip at 1969 MeV/c is deeper than that at 2172 MeV/c.

The second peak is broad at lower momentum, and becomes narrower and smaller

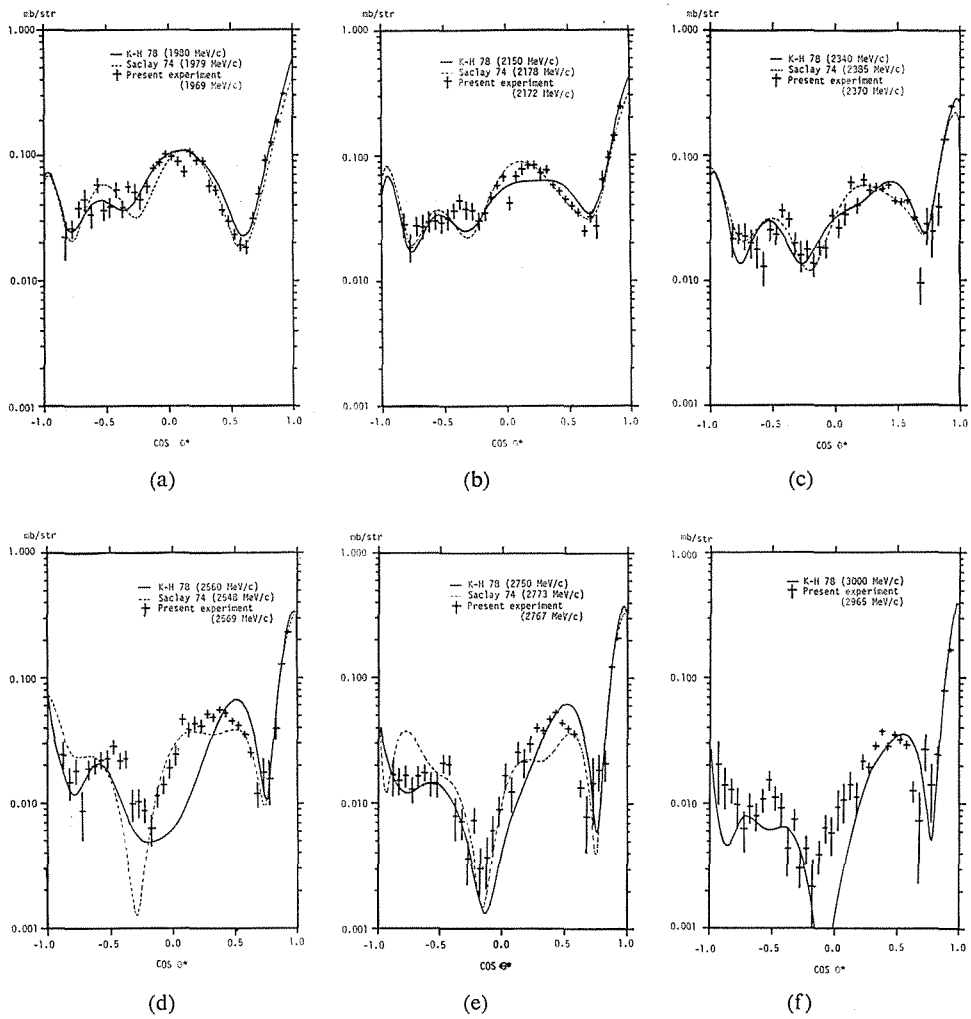

Fig. V–1–a)–f). Differential cross sections. The solid and dashed curves indicate the results by K–H 78[4] and Saclay 74[2] analyses, respectively.

and moves forward as the beam momentum increases. The second dip becomes deep very rapidly as the beam momentum increases and is deeper than the first dip above 2370 MeV/c. The second dip clearly characterizes the aspects of the differential cross section of charge exchange scattering at higher momentum. The second dip sits around $\cos\theta^* = -0.2$ for all momental.

The third peak around $\cos\theta^* = -0.5$ is smaller and weaker than the second peak. Increasing the incident pion momentum, the position of the third peak moves backward slightly and the height of the peak becomes lower. The depth of the third dip is approximately the same as that of the first dip. Although the statistics are poor in the backward region because of the rather small acceptance of the detector, the third peak seems to be weak at 2767 MeV/c, but it becomes clear again at 2965 MeV/c.

The backward peak is out of the acceptance of the detector which is limited at around $\cos\theta^* = -0.9$.

V–1. Comparison with other data

The most recent systematic measurements with high statistic on the $\pi^-p \to \pi^0 n$ charge exchange differential cross sections are those by Nelson *et al.*[6] and by Brown *et al.*[7]

Nelson *et al.* measured the cross section at six momenta between 1030 MeV/c and 2390 MeV/c using optical spark chambers. Their results at 1990 MeV/c, 2190 MeV/c and 2390 MeV/c overlap to the present experiment. Brown *et al.* measured the cross section at 22 momenta between 618 MeV/c and 2724 MeV/c using the scintillation hodoscopes for π^0 mesons and the liquid scintillation counters for neutrons. The measurements at 1975 MeV/c and 2724 MeV/c also overlap to the present measurements.

The present results are in agreement with their results as a whole as is seen in

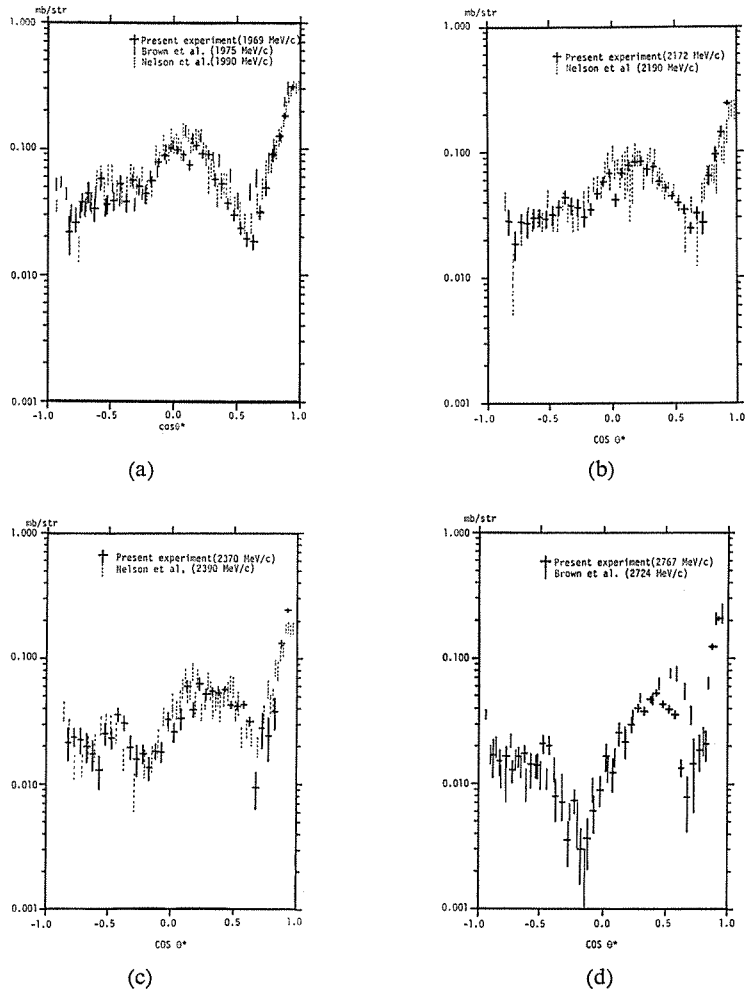

Fig. V–2–a–d). Differential cross sections.
+ shows the present results. | shows those by Nelson *et al*[6]. | shows those by Brown *et al*[7].

Fig. V–2–a)–d). However, at 1969 MeV/c some discrepancies are seen in the angular region between $\cos\theta^*=0.3$ and 0.7. In this region the present experiment yields lower differential cross sections than that of Brown *et al.* The discrepancy with Nelson *et al.* is very small. At 2172 MeV/c the present results are in good agreement with Nelson *et al.* At 2370 MeV/c the present experiment yields higher forward differential cross section than that of Nelson *et al.* At 2767 MeV/c there is a noticeable disagreement between the present results and those of Brown *et al.* in the angular region between $\cos\theta^*=0.4$ and 0.7. But it should be noted that the incident pion momentum of Brown *et al.* differs from that of the present experiment by 43 MeV/c.

In general the present results give smaller differential cross sections around $\cos\theta^*=0.5$ than those of Brown *et al.*

V–2. Comparison with predictuions of the partial wave analyses

The most recent partial wave analyses were performed at Saclay 74[2] (up to 2.8 GeV/c), at CMU–LBL 78[3] (up to 2.0 GeV/c), at Karlsruhe-Helsinki 78[4] (up to 10 GeV/c) and by Hendry[5] (from 1.6 GeV/c to 10 GeV/c). The predictions of the Saclay 74 and the Karlsruhe-Helsinki 78 (K–H 78) analyses can be compared with the present results and plotted in Fig. V–1–a)–f).

These analyses can reproduce the present results in some extent. At 1969 MeV/c and 2172 MeV/c, both analyses of the Saclay 74 and the K–H 78 well reproduce the present results. Between 2370 MeV/c and 2767 MeV/c, there are notable discrepancies among those two predictions in the angular region of $\cos\theta^*=0.0$ to $\cos\theta^*=0.7$. In this region the present results seem to have somewhat better agreement with the Saclay 74 results than the K–H results because the K–H 78 analysis includes the results by Brown *et al.* which yielded higher differential cross sections than ours.

In the backward region at 2767 MeV/c, the K–H 78 analysis reproduce our results fairly well. The peak around $\cos\theta^*=-0.8$ predicted by the Saclay 74 analysis does not appear in our results. At 2965 MeV/c the K–H analysis cannot predict the peak appeared around $\cos\theta^*=-0.5$ of our results.

Chi-squares for these partial wave analyses were calculated and are tabulated in Table V–2. In the lower momentum region from 1969 MeV/c to 2370 MeV/c, these analyses give small χ^2's. In the higher momentum region above 2569 MeV/c, although the both analysis give rather large χ^2's, the Saclay 74 analysis is some what better than the K–H 78 analysis.

As a whole χ^2's calculated with the Saclay 74 analysis are smaller than those with the K–H 78 analysis.

Table V–2. χ^2_ν's calculated by the differential cross sections of the present experiment and those of the partial wave analyses.

	1969 MeV/c	2172 MeV/c	2370 MeV/c	2569 MeV/c	2767 MeV/c	2965 MeV/c
Saclay 74	4.77	3.50	3.99	6.64	14.29	
Karlsruhe-Helshinki 78	3.76	3.77	4.88	17.16	16.09	9.09
CMU–LBL 78	5.67					

V–3. Legendre polynominal expansion

The differential cross sections can be expanded in terms of the Legendre polynomial function,

$$\frac{d\alpha}{d\Omega}=\frac{1}{q^2}\sum_{n=0} A_n P_n(\cos\theta)\,.$$

These Legendre coefficients A_n's are also expressed in terms of partial wave amplitudes[22] as follows,

$$A_n=\mathrm{Re}\sum_{l,m}[\rho_{nlm}\alpha_l\alpha_m^*+\sigma_{nlm}\beta_l\beta_m^*]$$

where

$$\rho_{nlm}=\frac{2n+1}{2}\int_{-1}^{1} P_n(z)\,P_l(z)\,P_m(z)dz\,,$$
$$\sigma_{nlm}=\frac{2n+1}{2}\int_{-1}^{1} P_n(z)\,P_l'(z)\,P_m'(z)dz\,,$$

There are recurrence formulae for ρ and σ.

$$\rho_{n,l+1,m}=\frac{2l+1}{l+1}\frac{1}{2m+1}[(m+1)\rho_{n,l,m+1}+m\rho_{n,l,m-1}]-\frac{l}{l+1}\rho_{n,l-1,m}$$

$$\sigma_{n,l+1,m}=\frac{2l+1}{l}\frac{1}{2m+1}[m\sigma_{n,l,m+1}+(m+1)\sigma_{n,l,m-1}]-\frac{l+1}{l}\sigma_{n,l-1,m}\,,$$

with the starting value,

$$\rho_{n,0,m}=\delta_{n,m},\qquad \rho_{n,1,m}=\frac{n+1}{2n+3}\delta_{n,m-1}+\frac{n}{2n-1}\delta_{n,m+1}\,,$$
$$\sigma_{n,0,m}=0,\qquad \sigma_{n,1,m}=\frac{(n+1)(n+2)}{2n+3}\delta_{n,m-1}+\frac{n(n-1)}{2n-1}\delta_{n,m+1}\,,$$

α_l and β_l are the coefficients of the expansion of spin flip and non-flip amplitudes, respectively,

$$qG=\sum_{l=0}^{\infty}\alpha_l P_l(z)\,,\qquad qH=\sum_{l=1}^{\infty}\beta_l\sin\theta P_l'(z)\,,$$
$$\alpha_l=(l+1)T_{l+}+lT_{l-}\,,\qquad \beta_l=T_{l+}-T_{l-}\,,$$

where $l\pm$ belongs to $J=l\pm1/2$ and $T_{l\pm}$ represents partial wave amplitudes. Decomposition of A_n up to $l=7$ are listed in Table V–3. The symbol in the left hand side column, for example S_1P_1, indicates $\mathrm{Re}\,(S_{1/2}P_{1/2}^*)$. The numbers listed in the tables are weights of these real part combination. The coefficient A_n's correlate to the special partial wave amplitudes as is seen in Table V–3. Therefore, the behaviors of these Legendre coefficients provide useful information on the resonances through the corresponding partial waves.

The Legendre coefficients A_n's were calculated from the present results. The order of the polynomial expansions needed to represent the differential cross sections was tested by the reduced chi-square χ_ν^2 as a function of the order of expansion. Fig. V–3 shows the variation of χ_ν^2. As is shown in Fig. V–3, at low momenta of 1969 MeV/c and 2172 MeV/c, the χ_ν^2 becomes constant above $n=8$. At these low momenta the order of the expansion of $n=8$ should be enough. However, in order to

Table V–3. Decomposition of the coefficients of the Legendre polynominal expansion of the differential cross sections to the partial wave amplitudes up to $l=7$.

	A_0	A_1	A_2	A_3	A_4	A_5	A_6	A_7	A_8	A_9	A_{10}	A_{11}	A_{12}	A_{13}	A_{14}
$S_1\ S_1\ +P_1\ P_1$	1.0														
$S_1\ P_1$		2.0													
$S_1\ P_3\ +P_1\ D_3$		4.0													
$S_1\ D_3\ +P_1\ P_3$			4.0												
$S_1\ D_5\ +P_1\ F_5$			6.0												
$S_1\ F_5\ +P_1\ D_5$				6.0											
$S_1\ F_7\ +P_1\ G_7$				8.0											
$S_1\ G_7\ +P_1\ F_7$					8.0										
$S_1\ G_9\ +P_1\ H_9$					10.0										
$S_1\ H_9\ +P_1\ G_9$						10.0									
$S_1\ H_{11}+P_1\ I_{11}$						12.0									
$S_1\ I_{11}\ +P_1\ H_{11}$							12.0								
$S_1\ I_{13}\ +P_1\ K_{13}$							14.0								
$S_1\ K_{13}\ +P_1\ I_{13}$								14.0							
$S_1\ K_{15}$								16.0							
$P_3\ P_3\ +D_3\ D_3$	2.0		2.0												
$P_3\ D_3$		0.8		7.2											
$P_3\ D_5\ +D_3\ F_5$		7.2		4.8											
$P_3\ F_5\ +D_3\ D_5$			1.7		10.3										
$P_3\ F_7\ +D_3\ G_7$			10.3		5.7										
$P_3\ G_7\ +D_3\ F_7$				2.7		13.3									
$P_3\ G_9\ +D_3\ H_9$				13.3		6.7									
$P_3\ H_9\ +D_3\ G_9$					3.6		16.4								
$P_3\ H_{11}+D_3\ I_{11}$					16.4		7.6								
$P_3\ I_{11}\ +D_3\ H_{11}$						4.6		19.4							
$P_3\ I_{13}\ +D_3\ K_{13}$						19.4		8.6							
$P_3\ K_{13}\ +D_3\ I_{13}$							5.6		22.4						
$P_3\ K_{15}$							22.4		9.6						
$D_5\ D_5\ +F_5\ F_5$	3.0		3.4		2.6										
$D_5\ F_5$		0.5		3.2		14.3									
$D_5\ F_7\ +F_5\ G_7$		10.3		8.0		5.7									
$D_5\ G_7\ +F_5\ F_7$			1.1		4.7		18.2								
$D_5\ G_9\ +F_5\ H_9$			14.3		9.4		6.4								
$D_5\ H_9\ +F_5\ G_9$				1.8		6.2		22.0							
$D_5\ H_{11}+F_5\ I_{11}$				18.2		10.8		7.0							
$D_5\ I_{11}\ +F_5\ H_{11}$					2.5		7.6		25.8						
$D_5\ I_{13}\ +F_5\ K_{13}$					22.0		12.2		7.8						
$D_5\ K_{13}+F_5\ I_{13}$						3.2		9.1		29.6					
$D_5\ K_{15}$						25.8		13.7		8.5					
$F_7\ F_7\ +G_7\ G_7$	4.0		4.8		4.2		3.0								
$F_7\ G_7$		0.4		2.2		6.6		22.8							
$F_7\ G_9\ +G_7\ H_9$		13.3		10.9		9.2		6.5							
$F_7\ H_9\ +G_7\ G_9$			0.9		3.2		8.5		27.4						
$F_7\ H_{11}+G_7\ I_{11}$			18.2		12.6		10.2		7.0						
$F_7\ I_{11}\ +G_7\ H_{11}$				1.4		4.3		10.4		31.9					
$F_7\ I_{13}\ +G_7\ K_{13}$				22.8		14.4		11.2		7.6					
$F_7\ K_{13}+G_7\ I_{13}$					2.0		5.4		12.2		36.4				
$F_7\ K_{15}$					27.4		16.2		12.2		8.1				
$G_9\ G_9\ +H_9\ H_9$	5.0		6.1		5.7		4.9		3.4						
$G_9\ H_9$		0.3		1.7		4.6		10.7		32.7					
$G_9\ H_{11}+H_9\ I_{11}$		16.4		13.7		12.3		10.4		7.3					
$G_9\ I_{11}\ +H_9\ H_{11}$			0.7		2.5		6.0		13.0		37.8				
$G_9\ I_{13}\ +H_9\ K_{13}$			22.0		15.7		13.5		11.1		7.7				

Table V–3 (continued).

	A_0	A_1	A_2	A_3	A_4	A_5	A_6	A_7	A_8	A_9	A_{10}	A_{11}	A_{12}	A_{13}	A_{14}
$G_9\ K_{13}+H_9\ I_{13}$				1.1		3.4		7.4		15.2		42.9			
$G_9\ K_{15}$				27.4		17.7		14.7		11.9		8.2			
$H_{11}H_{11}+I_{11}\ I_{11}$	6.0		7.3		7.1		6.4		5.4		3.8				
$H_{11}I_{11}$		0.3		1.4		3.6		7.6		15.5		43.6			
$H_{11}I_{13}+I_{11}\ K_{13}$		19.4		16.4		15.2		13.6		11.4		7.9			
$H_{11}K_{15}+I_{11}\ I_{13}$			0.6		2.1		4.7		9.3		18.1		49.3		
$H_{11}K_{15}$			25.8		18.7		16.5		14.6		12.1		8.3		
$I_{13}\ I_{13}+K_{13}\ K_{13}$	7.0		8.6		8.4		7.9		7.1		5.9		4.1		
$I_{13}\ K_{13}$		0.2		1.2		3.0		6.1		11.2		20.9		55.5	
$I_{13}\ K_{15}$		22.4		19.2		18.0		16.7		14.9		12.4		8.5	
$K_{13}\ K_{15}$			0.5		1.8		3.9		7.4		13.0		23.7		61.6
$K_{15}\ K_{15}$	8.0		9.9		9.7		9.3		8.6		7.7		6.4		4.4

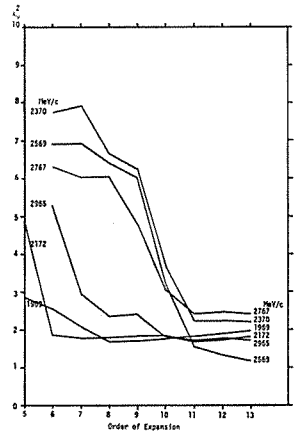

Fig. V–3. χ^2_p as the function of the order of the Legendre polynominal expansion.

compare these coefficients with those of K–H 78[22] the order of the expansion of $n=11$ was chosen in each momentum even in the lower momenta. The coefficients of A_0 to A_8 in the lower momenta for the expansion of both order 8 and of order 11 almost coincide with each other.

Because the data region are limited between $\cos\theta^*=-0.9$ to 0.95 the Legendre polynomial fits of our data alone gave unstable behavior in the forward and backward region. In order to avoid those behavior the backward (180°) and forward (0°) data by Kistiakovsky 72[12] and the prediction of K–H 78 partial wave analysis, respectively, were added to our data. The errors of these data were assumed to be 10%.

The results of the Legendre polynomial expansion are listed in Table V–4 and are plotted in Fig. V–4–a)–c) together with the prediction of both K–H 78 and Saclay 74 (part of data) partial wave analyses. The Legendre expansion of the differential cross sections by Brown *et al.* was executed by Höhler *et al.*[22] up to higher order coefficients. These results are also shown in Fig. V–4. In the low momentum region, the results of Brown *et al.* and those of ours are in good agreement as a whole. In the high momentum region, large discrepancies were found in the coefficients of A_3, A_4 and A_7.

Table V–4. Coefficients of the Legendre polynominal expansions of the differential cross sections $d\sigma/d\Omega=(1/q^2)\sum_{n=0}^{n=11} A_n P_n(\cos\theta)$.

Momentum (MeV/c) Coefficient	1969 MeV/c	2172 MeV/c	2370 MeV/c
A_0	0.142±0.005	0.129±0.004	0.098±0.005
A_1	0.139±0.013	0.124±0.009	0.126±0.014
A_2	0.117±0.020	0.090±0.014	0.089±0.020
A_3	0.209±0.020	0.133±0.025	0.130±0.021
A_4	0.254±0.022	0.193±0.014	0.130±0.019
A_5	0.158±0.019	0.146±0.014	0.155±0.017
A_6	0.042±0.020	0.048±0.013	0.077±0.013
A_7	−0.019±0.021	−0.035±0.014	−0.054±0.016
A_8	0.042±0.020	−0.014±0.014	−0.059±0.019
A_9	0.019±0.025	−0.004±0.017	−0.106±0.023
A_{10}	−0.002±0.020	−0.021±0.014	−0.038±0.020
A_{11}	0.003±0.021	−0.037±0.015	−0.116±0.021
Total cross section (mb)	0.939±0.036	0.755±0.021	0.522±0.028

Momentum Mev/c) Coefficient	2569 MeV/c	2767 MeV/c	2965 MeV/c
A_0	0.105±0.003	0.094±0.003	0.081±0.003
A_1	0.115±0.007	0.121±0.008	0.115±0.007
A_2	0.132±0.009	0.160±0.012	0.177±0.010
A_3	0.100±0.010	0.121±0.013	0.130±0.011
A_4	0.159±0.010	0.170±0.013	0.187±0.014
A_5	0.142±0.011	0.178±0.014	0.177±0.014
A_6	0.099±0.011	0.143±0.014	0.167±0.015
A_7	−0.061±0.010	−0.015±0.013	0.052±0.014
A_8	−0.074±0.010	−0.063±0.014	−0.006±0.014
A_9	−0.070±0.012	−0.088±0.016	−0.031±0.015
A_{10}	−0.080±0.012	−0.067±0.014	−0.044±0.012
A_{11}	−0.072±0.013	−0.045±0.015	−0.020±0.012
Total cross section (mb)	0.506±0.013	0.413±0.015	0.329±0.011

There are some structures on A_3, A_4, A_7, A_8, A_9, A_{10} and A_{11} in the mass range of 2150 MeV and 2550 MeV of the present experiment. Higher order coefficients especially above A_8 have a clearer dip than the lower one. These structures imply the existence of the high spin resonances in that region, for example H_{311} (2416) *etc.*

The value of χ^2 for each coefficient is listed in Table V–5. The χ^2 increases rapidly above 2569 MeV/c in the case of both K–H 78 and Saclay 74, as is already seen in the comparison with the differential cross sections in Chapter V–2.

There are some characteristic features in these individual coefficients. At the momenta of 1969 MeV/c to 2370 MeV/c, the coefficients of A_2, A_{10} and A_{11} of the K–H analysis and those of A_1, A_3, A_9 and A_{10} of the Saclay 74 analysis disagree with our results. At the momenta above 2569 MeV/c, the coefficients of A_1, A_2, A_3, A_6, A_7, A_{10} and A_{11} of the K–H 78 analysis and those of A_2, A_8 and A_{11} of the Saclay 74 analysis disagree with our results. However, the discrepancies at the momenta

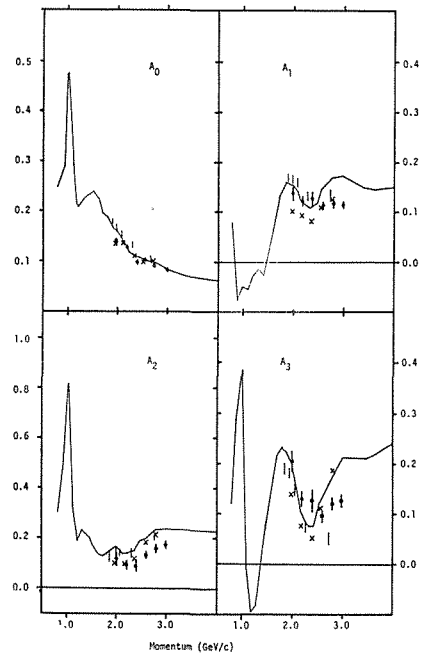

(a)

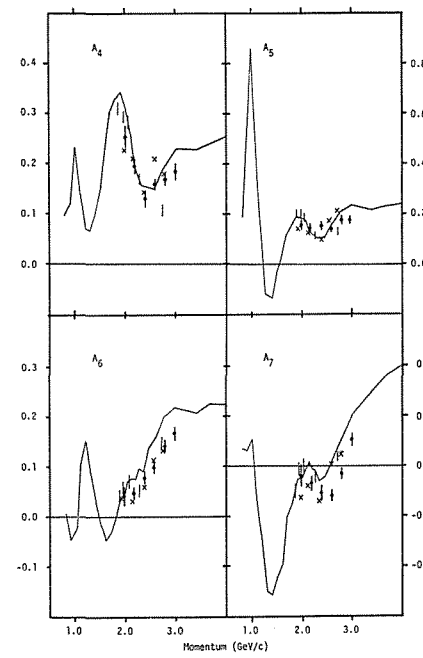

(b)

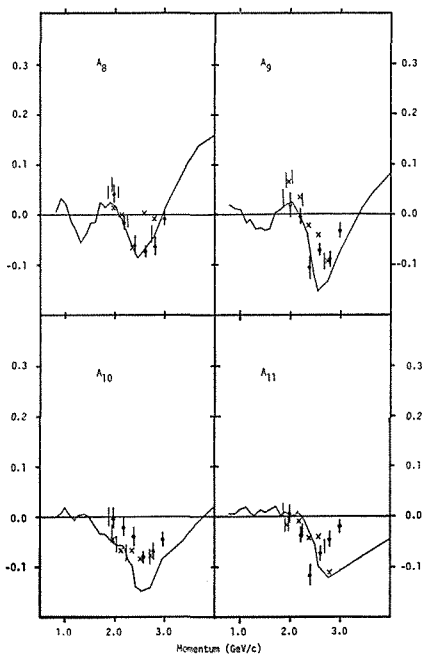

(c)

Fig. V–4–a)–c).
Coefficients of the Legendre polynomial expansion of the differential cross section. The solid curves indicate the predictions by K–H 78. ×'s indicate the prediction by Saclay 74. ○ and | indicate the present results and those by Brown *et al.*[7),22)], respectively.

of 1969 MeV/c to 2370 MeV/c are not so large comparing with those at the momenta above 2569 MeV/c. Therefore, the behaviors of these coefficients at the momenta above 2569 MeV/c must be examined. According to the decomposition of the

Table V–5. χ^2's calculated by the coefficients of the Legendre polynominal expansions of the present experiment and those of the partial wave analyses.

Karlsruhe-Helshinki 78

Momentum (MeV/c) A_n	1980	2150	2340	2560	2750	3000
0	7.56	0.68	8.46	1.00	11.11	3.57
1	0.94	0.38	1.11	25.00	36.43	66.20
2	2.79	15.15	8.93	49.78	32.02	29.61
3	0.23	0.16	4.50	4.41	10.24	49.00
4	5.59	1.06	2.54	0.64	2.90	9.14
5	1.21	0.08	5.80	0.12	2.50	13.77
6	0.06	8.12	1.52	31.20	19.88	13.86
7	0.10	9.00	1.23	30.25	20.35	12.80
8	1.60	0.14	0.10	0.02	1.17	3.16
9	0.02	0.24	3.72	48.70	8.78	7.19
10	6.02	6.67	8.86	33.32	30.36	10.99
11	0.11	8.92	18.52	2.67	24.63	51.18

Saclay 74

Momentum (MeV/c) A_n	1979	2178	2385	2548	2773
0	2.14	0.35	4.37	0.09	5.44
1	9.36	10.71	10.28	0.23	1.07
2	0.75	0.29	2.38	36.67	22.16
3	11.32	13.17	12.41	2.72	27.27
4	1.72	1.15	0.21	26.01	0.76
5	0.80	3.33	10.68	12.33	5.76
6	0.03	1.78	2.70	2.07	0.66
7	5.02	0.03	1.22	38.13	8.13
8	2.29	1.29	0.09	54.62	16.84
9	3.64	5.28	13.17	5.51	0.21
10	5.21	11.28	1.95	0.30	0.20
11	1.28	3.05	11.06	5.32	21.26

Legendre coefficient into the partial wave amplitudes listed in Table V–3, the low order coefficients A_0, A_1, A_2, A_3 are mainly contributed by the products of low angular momentum waves by low angular momentum waves and the products of large angular momentum waves by large angular momentum waves. The coefficients A_4, A_5, A_6, A_7 are mainly contributed by the products of low angular momentum waves by large angular momentum waves. Finally, the coefficients A_8, A_9, A_{10}, A_{11} are contributed by only the products of large angular momentum waves by large angular momentum waves.

In this momentum region, the large angular momentum waves, such as G_7, G_9, H_9, H_{11}, I_{11} and so on, start to play important roles. In order to discuss somewhat qualitatively the contributions of these large angular momentum waves to the Legendre coefficients A_n's, the coefficients for these partial wave amplitudes which come into each Legendre coefficient were calculated at the momentum of 2.8 GeV/c for K–H 78 and Saclay 74 analyses and shown in Fig. V–5–a)–b). As is seen in this figure, the G_9 and H_{11} and possibly H_9 and I_{11} waves of the K–H 78 analysis have rather large contributions to the Legendre coefficients of A_{10} and A_{11}. Although the I_{13} and K_{13} waves have large coefficients for A_{10} and A_{11}, their contributions are small, because the amplitudes themselves are small. These four G, H and I waves also have con-

tributions to the Legendre coefficients of different order other than A_{10} and A_{11}. As is seen in Fig. V–5, the Legendre coefficients A_0, A_4, A_5 and A_8 are well coincide with the K–H 78 prediction and the deviation of A_1, A_2, A_3 and A_6, A_7 have a different

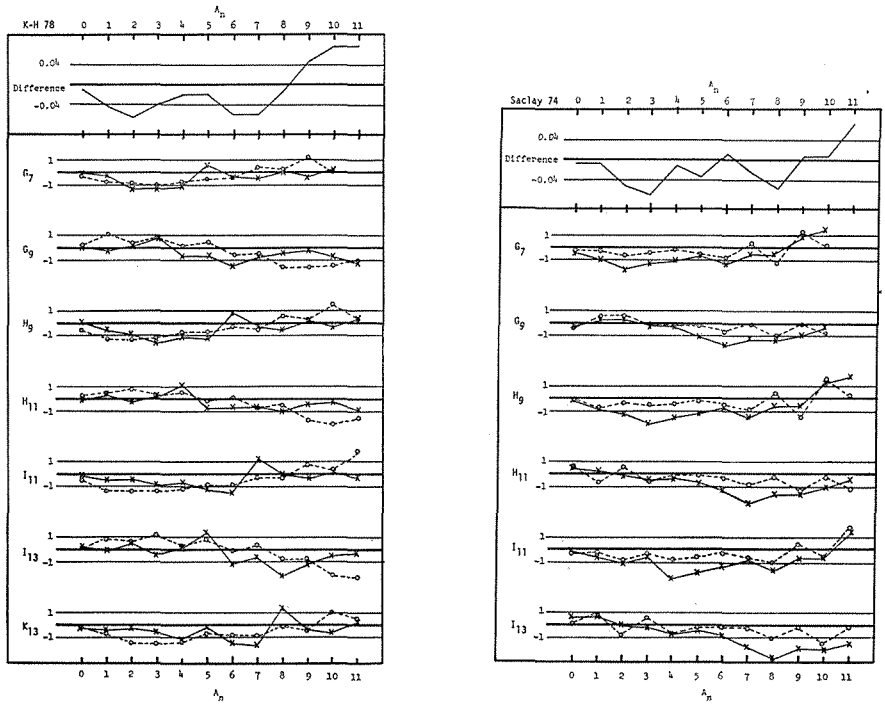

Fig. V–5–a)–b). Decomposition of Legendre coefficients of the K–H 78 and the Saclay 74 phase shifts. The top figure shows the difference of the Legendre coefficient with those of the present results as a function of n. The rest of figure indicates the coefficients for the large angular momentum waves which come in each Legendre coefficient. Solid lines indicate coefficients for the real part of the partial waves. Dashed lines indicate those for the imaginary part.

sign than those of A_{10} and A_{11}. Therefore, in order to improve the discrepancies in these Legendre coefficients, it seems to be sensible to modify the combination of at least two or more waves among the G_9, H_9, H_{11}, I_{11} waves.

Predictions of Saclay 74 analysis on the Legendre coefficients are somewhat different than those of K–H 78 analysis, because the Saclay 74 phase shifts includes the partial waves up to only $l=7$, while the K–H 78 phase shifts includes the waves up to $l=9$. Furthermore, the Saclay 74 analysis is limited below 2773 MeV/c, so neither qualitative nor quantitative discussions are useful in this momentum.

The present experimental results are expected to give a tight constraint for a future phase shift analysis to determine the large angular momentum waves and the high spin resonances together with the results of the new polarization parameters.[14]

Total cross sections were obtained by the Legendre coefficient of A_0. These results are shown in Fig. V–6 with other early experimental results. The agreement

with other experiments are good as a whole except for the results by Carrol *et al.*[10] which give smaller values below 2 GeV/c. The present results give somewhat smaller total cross sections than those of Brown *et al.*[7] systematically. Especially the discrepancy becomes large in the higher momentum region.

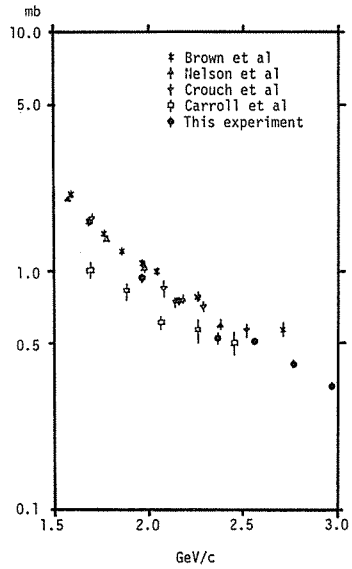

Fig. V–6. Total cross sections of the $\pi^- p \to \pi^0 n$ charge exchange scattering. The results of other early experiments are also shown.[6),7),10),11)]

V–4. Comparison with a Regge pole model

As is well known, Regge pole models well predict the forward and backward

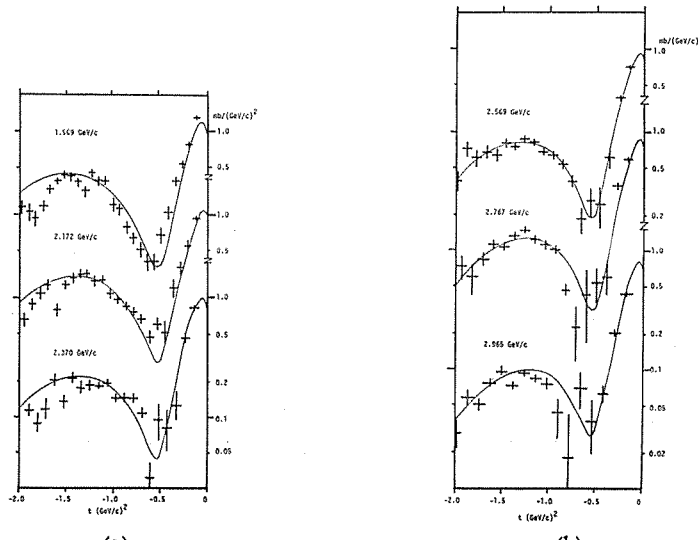

(a) (b)

Fig. V–7–a)–b). Forward differential cross sections together with the prediction of the Regge pole model.

differential cross sections in the high energy region above about 5 GeV/c. The forward steep peak and the first dip appeared in the charge exchange cross section can be understood by the t-channel exchange of $I=1$ poles, while the forward peaks in the elastic scattering of $\pi^\pm p$ are understood by the t-channel exchange of $I=1$ and $I=0$ poles. V. Barger and R. J. N. Phillips[23] calculated πN scattering amplitudes above 5 GeV/c, at the forward angular range of $0\leq -t\leq 2$ (GeV/c)^2, in terms of P, P', P'', ρ and ρ' Regge poles. The present results were compared with this analysis by extrapolating above Regge amplitudes, as are shown in Fig. V–7–a)–b). A good agreement is obtained except below 2.37 GeV/c and in the large momentum transfer region of $|t|>1.7$.

V–5. Conclusion

The present results of the differential cross sections are in good agreement with experimental results by Nelson *et al.* There are notable discrepancies around $\cos\theta^*=0.5$ between the present results and those of Brown *et al.* The predictions of the partial wave analyses of Saclay 74 and K–H 78 well reproduce the present results at 1969 MeV/c and 2172 MeV/c. However, both analyses cannot reproduce the present results above 2370 MeV/c. The results of the Legendre expansion seem to indicate that the large angular momentum waves such as G_9, H_9, H_{11} and I_{11} waves must be carefully determined with a new partial wave analysis including the present results to establish the high spin πN resonances in this energy region. The forward differential cross sections are well reproduced with the Regge pole amplitudes in the region of $|t|<1.7$.

ACKNOWLEDGEMENT

The author would like to express his sincere thanks to Prof. K. Miyake and Prof. T. Nakamura for their continuous encouragements and guidances throughout this work. He is deeply grateful to Prof. M. Kobayashi, Dr. R. Kikuchi, Dr. Y. Hemmi, Dr. N. Sasao, Dr. I. Nakano, Dr. M. Daigo, Mr. M. Minowa, Mr. T. Adachi, Mr. S. Naito and Mr. M. Sakuda for their advices and collaboration in carrying out this experiment.

The present experiment performed as the first counter experiment at KEK. Therefore, he is indebted to most of personnel at KEK, such as the members of the machine operation division headed by Prof. Y. Kojima for the stable operation of the proton synchrotron, to those of the beam channel division headed by Prof. A. Kusumegi for constructing and tuning the pion beam line, to those of the counter division headed by Prof. Y. Nagashima for assistance in preparing a liquid hydrogen target, multiwire spark chambers and electronics, to those of the data handling division headed by Prof. H. Yoshiki for developing the fast on-line system and assistance in off-line data analysis and to those of the work shop headed by Prof. T. Hongo for assistance in mechanical constructions and fabrications of the detector.

REFERENCES

1) R. J. Cashmor, *Proceeding of the 19th International Conference on High Energy Physics, Tokyo,* 1978, p 811.

J. L. Rosner, Phys. Report **11** (1974) 189.
R. Hörgan and R. H. Dalitz, Nucl. Physics **B66** (1973) 135.
2) R. Ayed and P. Bareyre, Phys. Letters **50B** (1974) 1 (Rev. of Particle Properties).
3) R. E. Cutkofsky *et al., Contributed paper to the 19th International Conference on High Energy Physics, Tokyo,* 1978, No. 799.
Phys. Rev. Letters **37** (1976) 645.
4) E. Pieterinen, Phys. Letters **75B** (1978) 1 (Rev. of Particle Properties).
G. Höhler *et al.*, TKP 78–11, TKP 78–12.
5) A. W. Hendry, LBL–7524.
6) J. E. Nelson, LBL–1091 (*Ph. D. Thesis*).
J. E. Nelson *et al.*, Phys. Letters **47B** (1973) 281.
7) R. M. Brown *et al.*, Nucl. Physics **B117** (1976) 12, Nucl. Physics **B137** (1978) 542.
8) S. R. Shannon *et al.*, Phys. Rev. Letters **33** (1974) 237.
9) R. M. Brown *et al.*, Nucl. Physics **B144** (1978) 287.
10) A. S. Carrol *et al.*, Phys. Rev. **177** (1969) 2047.
11) H. R. Crouch *et al.*, Phys. Rev. Letters **21** (1968) 849.
12) V. Kistiakovsky *et al.*, Phys. Rev. **D6** (1972) 1882.
13) P. Borgeaud *et al.*, Phys. Letters **10** (1964) 137.
V. V. Barmin *et al.*, Soviet Journal of Nucl. Physics **4** (1967) 592.
W. S. Risk, Phys. Rev. **167** (1968) 1249.
M. A. Wahling *et al.*, Phys. Rev. **168** (1968) 1515.
V. D. Antopolsky *et al.*, Phys. Letters **28B** (1968) 223.
V. Kistiakovsky *et al.*, Phys. Rev. Letters **22** (1969) 618.
R. C. Chase *et al.*, Phys. Rev. Letters **22** (1969) 1137.
R. C. Chase *et al.*, Phys. Rev. **D2** (1970) 2588.
C. DeMerzo *et al.*, Phys. Letters **56B** (1975) 487.
D. D. Drobnis *et al.*, Phys. Rev. Letters **20** (1968) 274.
14) M. Minowa, Memoirs of the Faculty of Science, Kyoto University, Series of Physics, Astrophysics, Geophysics and Chemistry, **36**, (1981) 109.
15) T. Adachi, *ibid.* **36** (1981), 169.
16) V. Perez-Mendez and J. M. Pfab, Nucl. Instr. and Methods **33** (1965) 141.
V. Perez-Mendez *et al.*, Nucl. Instr. and Methods **46** (1967) 197.
T. Tsuru *et al.*, KEK-EXP Facil. **5** (1976).
17) J. Fischer and S. Shibata, IEEE of Trans. of Nucl. Science **15** (1968) 572.
O. C. Allkofer *et al.*, Nucl. Instr. and Methods **79** (1970) 181.
18) D. D. Briggs *et al.*, Nucl. Instr. and Methods **95** (1971) 377.
19) D. F. Crawford and H. Messel, Phys. Rev. **128** (1962) 2352, "Electron-Photon Shower Distribution Function Table" (1970).
20) Y. Yoshimura *et al.*, Nucl. Instr. and Methods **126** (1975) 541.
21) Y. Asano *et al.*, (*Submited for publication in* Nucl. Instr. and Methods).
22) G. Höhler *et al.*, TKP 78–10.
23) V. ×Barger and R. J. N. Phillips, Phys. Rev. **187** (1969) 2210.